THE NATURE OF DUST IN COMPACT GALACTIC PLANETARY NEBULAE FROM *SPITZER* SPECTRA[*]

Letizia Stanghellini[1], D. A. García-Hernández[2,8], Pedro García-Lario[3], James E. Davies[4], Richard A. Shaw[5], Eva Villaver[6], Arturo Manchado[2,9], and Jose V. Perea-Calderón[7]

[1] National Optical Astronomy Observatory, Tucson, AZ 85719, USA; lstanghellini@noao.edu
[2] Instituto de Astrofísica de Canarias, Vía Láctea s/n, La Laguna, E-38200 Tenerife, Spain; agarcia@iac.es, amt@iac.es
[3] Herschel Science Centre, European Space Astronomy Centre, Research and Scientific Support Department of ESA, Villafranca del Castillo, P.O. Box 50727, E-28080 Madrid, Spain; Pedro.Garcia-Lario@sciops.esa.int
[4] Spitzer Science Center, Infrared Processing and Analysis Center, California Institute of Technology, 1200 East California Boulevard, Pasadena, CA 91125, USA; jdavies@ipac.caltech.edu
[5] National Optical Astronomy Observatory, 950 N. Cherry Av., Tucson, AZ 85719, USA; shaw@noao.edu
[6] Departamento de Física Teórica C-XI, Universidad Autónoma de Madrid, E-28049 Madrid, Spain; eva.villaver@uam.es
[7] European Space Astronomy Centre, INSA S. A., P.O. Box 50727, E-28080 Madrid, Spain; Jose.Perea@sciops.esa.int

Received 2011 August 10; accepted 2012 May 8; published 2012 June 26

ABSTRACT

We present the *Spitzer*/Infrared Spectrograph (IRS) spectra of 157 compact Galactic planetary nebulae (PNe). These young PNe provide insight on the effects of dust in early post-asymptotic giant branch evolution, before much of the dust is altered or destroyed by the hardening stellar radiation field. Most of the selected targets have PN-type IRS spectra, while a few turned out to be misclassified stars. We inspected the group properties of the PN spectra and classified them based on the different dust classes (featureless or F, carbon-rich dust or CRD, oxygen-rich dust or ORD, mixed-chemistry dust or MCD) and subclasses (aromatic and aliphatic, and crystalline and amorphous). All PNe are characterized by dust continuum and more than 80% of the sample shows solid-state features above the continuum, in contrast with the Magellanic Cloud sample where only ∼40% of the entire sample displays solid-state features; this is an indication of the strong link between dust properties and metallicity. The Galactic PNe that show solid-state features are almost equally divided among the CRD, ORD, and MCD. We analyzed dust properties together with other PN properties and found that (1) there is an enhancement of MCD PNe toward the Galactic center, in agreement with studies of Galactic bulge PNe; (2) CRD PNe could be seen as defining an evolutionary sequence, contrary to the ORD and MCD PNe, which are scattered in all evolutionary diagrams; (3) carbon-rich and oxygen-rich grains retain different equilibrium temperatures, as expected from models; and (4) ORD PNe are highly asymmetric, i.e., bipolar or bipolar core, and CRD PNe highly symmetric, i.e., round or elliptical; point symmetry is statistically more common in MCD than in other dust class PNe. By comparing the sample of this paper to that of Magellanic Cloud PNe, we find that the latter sample does not include MCD PNe, and the other dust classes are differently populated, with continuity of the fraction of F, CRD, ORD, and MCD populations from high to low metallicity environments. We also find similar sequences for CRD PNe in the Galactic disk and the Magellanic Clouds, except that the Magellanic Cloud PNe seem to attain higher dust temperatures at similar evolutionary stages, in agreement with the observational findings of smaller dust grains (i.e., lower radiation efficiency) in low metallicity interstellar environments.

Key word: planetary nebulae: general

Online-only material: color figures, extended figures, machine-readable tables

1. INTRODUCTION

Planetary nebulae (PNe) are the gas and dust envelopes ejected toward the end of the evolution of low- and intermediate-mass stars (LIMS, 1–8 $M_\odot$), at the tip of the thermally pulsing asymptotic giant branch (TP-AGB; e.g., Herwig 2005) phase. The stellar ejecta carries both the products of nucleosynthesis, such as carbon and nitrogen, and the α-elements, such as oxygen, neon, argon, and sulfur, whose net yields tend to be near zero in this mass range.

Dust may be fundamental to PN formation, since radiation pressure on the dust grains formed at the surface of AGB stars may be important in triggering the envelope ejection. PNe are ideal dust probes during their early evolutionary stages, since sputtering of the dust grains is expected to affect their dusty nature in their lifetime. Dust particles in PNe are typically cool (50–150 K) and radiate in the mid-infrared, producing a near-blackbody continuum spectrum (Cohen & Barlow 1974) that contributes to ∼40% of the total emergent flux (Zhang & Kwok 1991), and that peaks between 25 and 60 μm. *Spitzer* Infrared Spectrograph (IRS) spectroscopy has been very successful in tracing this dust component in PNe, as well as in a variety of other stellar targets including the AGB stars. Previous systematic PN studies based on IRS spectra include Galactic bulge (GO program 3633, Bobrowsky), halo (GO program 20049, Kwitter), disk (GTO program 30652, Bernard-Salas), and Magellanic Cloud (GTO program 103, Houck, and GO program 20443, Stanghellini) PNe. These data collectively show PN spectra with thermal dust continua, nebular emission lines, and a variety of dust signatures, with characteristics of carbon-rich and oxygen-rich compounds and different types of grains. From the comparative study of the different samples, some trends have

---

emerged: it appears that oxygen dust features, such as crystalline silicates, are more common in the bulge population (Gutenkunst et al. 2008; Perea-Calderón et al. 2009) than in the Galactic or Magellanic Cloud PNe (Stanghellini et al. 2007, hereafter S07; Bernard-Salas et al. 2009). In particular, in the Magellanic Cloud PNe, the oxygen and carbon dust features are never observed in the same spectrum. It is apparent that the galaxy metallicity has a strong effect on the nature of dust (S07; Bernard-Salas et al. 2009), and, from the Magellanic Cloud sample, it is apparent that PN bipolarity correlates strongly with oxygen-rich dust PNe (S07). Finally, gas and dust chemistry in Magellanic Cloud PNe are strongly correlated (S07).

What was lacking from the *Spitzer* database was a large, homogeneous sample of Galactic PN spectra, especially for young, unevolved PNe, to study the early dust features and their evolution across the Galactic disk. In this paper, we present the study of 157 Galactic angularly small targets classified as PNe, observed during the last cryogenic cycle of *Spitzer*. We collected the present sample to gain insight on the impact of dust and metallicity in stellar evolution, a fundamental question in astrophysics. The extensive target list is essential to explore the different dust types with statistical significance, and to study them across the Galactic disk, and in relation to the Galactic populations. The large sample presented here fills an important gap in the *Spitzer* program. Our compact Galactic PN data set is also complemented by a Wide Field Camera 3 (WFC3)/*Hubble Space Telescope* (*HST*) imaging survey of about one-third of the targets presented here. The morphological analysis, and that of the central stars (CSs) from the WFC3 data will complement the dust analysis presented here, allowing a much more detailed view on how dust affects the post-AGB and PN evolution in our galaxy compared to other environments.

Systematic comparison of IRS spectra of PNe belonging to different populations, such as the Galactic disk, halo, bulge, and the satellite galaxies, can address many key questions that have opened up in recent years regarding AGB stars as well. First, the absence of heavily obscured AGB stars in the Magellanic Clouds (Trams et al. 1999; Groenewegen et al. 2000; García-Hernández et al. 2009), in contrast with their Galactic counterparts (e.g., García-Hernández et al. 2006, 2007a), seems to indicate that, on average, lower metallicity environments such as those of the Magellanic Clouds are less favorable to dust production. The relative number of C-rich versus O-rich AGB stars in galaxies of the local group increases with decreasing metallicity (Cioni & Habing 2003; Cioni et al. 2003; Schultheis et al. 2004), which shows that mass-loss efficiency depends on metallicity (Höfner 2011).

In this paper, we present the 5–40 μm IRS spectra from *Spitzer* program GO 50261. In Section 2, we describe the target selection, exposures, and observing strategy. The data analysis, including spectral extraction, classification of the dust types, and continuum fitting, are presented in Section 3. In Section 4, we explore the relation of the dust characteristics with respect to other physical properties of the PNe in our sample, and in Section 5 we extend the comparison to PNe in the Magellanic Clouds. The summary and conclusions are in Section 6.

2. OBSERVATIONS

The aim of the target selection is to cover a homogenous and as much as possible complete set of compact Galactic PNe, most of which should be young. To this end, we selected PNe smaller than $4''$ in apparent size. Galactic PNe with diameters $<4''$ should be younger than $\sim 2.0 \times 10^3$ yr (Villaver et al. 2002a,

2002b), if they have heliocentric distances smaller than 6 kpc and if their expansion velocities are typical (20–40 km s^{-1}). Statistical distances (Stanghellini et al. 2008) help us distinguish which PNe are nearby and young from those that are distant and evolved. The population of spectroscopically confirmed Galactic PNe is listed either in the Strasbourg-ESO catalog of Galactic PNe (Acker et al. 1992) or in the MASH survey (Parker et al. 2006). Of the 1143 PN in the Strasbourg-ESO catalog, 143 are point sources, and 86 have $\theta < 4''$. The MASH survey gives another two PN with $\theta < 4''$ (but no point sources). From the 230 PNe thus selected, we explicitly eliminated the PNe already observed with *Spitzer*/IRS. Most of the exclusions are Galactic bulge and halo PNe, only 10 compact PNe in the Galactic disk had been observed with *Spitzer* before with similar observing configuration. Finally, we also exclude a dozen targets previously observed with *IRAS* or *Midcourse Space Experiment*. This filtering yielded a final sample of 157 compact Galactic PNe, which belong predominantly to the disk.

Twenty-six PNe in our sample may actually be bulge PNe. The fact that a PN belongs to the bulge rather than the disk is controversial, if for no other reason than that the Galactic PN distances are not known with high precision, and thus finding a PN in the direction of the bulge might not be sufficient to exclude it from the disk population. Stanghellini & Haywood (2010) made this selection for all Galactic PNe based on the best distance scale available, and included a brightness criterion, but uncertainties in the separation of the bulge to disk PN samples are of course possible. Furthermore, many of the PNe of our sample do not have a distance determined at all, given the lack of measurable angular diameter. Knowing the radial velocities of the targets could help, unfortunately at this time velocities are available only for a minority of the sample, and none for the PNe whose distances are not known.

Three PNe in our sample could belong to the Galactic halo. In Table 1, we list the observed targets with their IAU designation (Column 1), their common name (Column 2), and their equatorial coordinates (equinox 2000, Columns 3 and 4). In Columns 5 through 7 of Table 1, we list the IRS campaign number, the observing mode, and the exposure time, respectively. In the observing mode column, "0" is for the combination of SL (short–low, 5–14 μm) and LL (long–low, 14–40 μm) modules, and "1" for the combination of the SL, SH (short–high, 10–20 μm), and LH (long–high, 20–40 μm). Nearly all targets were observed with the SL module and "0" and "1" denote, respectively, whether the longer wavelength part of the spectra was observed at low or high resolution.

In Figure 1, we show the space distribution of our targets whose distance is known (92 PNe) compared with the general PN population (Stanghellini & Haywood 2010), where their distance from the Galactic plane is plotted against their radial distance from the Galactic center, and where we assume that the Galactic center is 8 kpc from the Sun. It is clear from this plot that the selected sample well represents the Galactic disk population of PNe. Most of the PNe in this study are actually young, being selected to be compact in apparent size.

We acquired, reduced, and analyzed the Galactic PN IRS/*Spitzer* spectra in a similar manner to that for Magellanic Cloud PNe (S07). Our astronomical observation request was built with the following requirements: (1) we aimed at obtaining 5–40 μm spectra, with different modes depending on the estimated PN brightness; and (2) we estimated the fluxes of our targets based on the upper limit provided by *IRAS* (Zhang & Kwok 1991). We chose the observing mode, computed the

Table 1
Observing Log

Name (1)	Alias (2)	α_{2000} (3)	δ_{2000} (4)	IRS Campaign (5)	Mode (6)	t_{exp} (s) (7)
PN G000.3−02.8	M 3-47	$17^h57^m52^s0$	$-30^d08^m15^s$	010600	0	44.04
PN G 000.6−01.3	Bl 3-15	$17^h52^m44^s1$	$-29^d12^m26^s$	010600	0	44.04
PN G000.6−02.3	H 2-32	$17^h56^m32^s8$	$-29^d43^m52^s$	010600	0	44.04
PN G000.8−01.5	Bl O	$17^h53^m49^s6$	$-28^d59^m10^s$	010600	1	12.58
PN G000.8−07.6	H 2-46	$18^h18^m47^s9$	$-32^d00^m23^s$	010600	0	12.58
PN G001.7−01.6	H 2-31	$17^h56^m10^s5$	$-28^d19^m58^s$	010600	0	44.04
PN G001.7−04.6	H 1-56	$18^h08^m03^s0$	$-29^d50^m17^s$	010600	0	12.58
PN G002.4−03.7	M 1-38	$18^h06^m05^s7$	$-28^d40^m28^s$	010600	1	12.58
PN G002.6−03.4	M 1-37	$18^h05^m25^s7$	$-28^d22^m03^s$	010600	1	12.58
PN G002.9−03.9	H 2-39	$18^h08^m14^s6$	$-28^d31^m54^s$	010600	0	44.04
PN G003.0−02.6	KFL 4	$18^h02^m59^s9$	$-27^d46^m46^s$	010600	0	44.04
PN G003.1+03.4	H 2-17	$17^h40^m07^s3$	$-24^d25^m41^s$	010600	1	12.58
PN G003.2−04.4	KFL 12	$18^h10^m39^s7$	$-28^d25^m06^s$	010600	0	44.04
PN G003.9−14.9	Hb 7	$18^h55^m48^s8$	$-32^d21^m23^s$	010700	0	12.58
PN G004.1−03.8	KFL 11	$18^h10^m20^s9$	$-27^d22^m19^s$	010600	0	44.04
PN G004.3−02.6	H 1-53	$18^h06^m05^s1$	$-26^d35^m30^s$	010700	0	44.04
PN G004.9−04.9	M 1-44	$18^h16^m17^s3$	$-27^d04^m31^s$	010600	1	12.58
PN G005.5+02.7	H 1-34	$17^h48^m07^s5$	$-22^d46^m46^s$	010600	1	12.58
PN G006.0+02.8	Th 4- 3	$17^h48^m37^s3$	$-22^d16^m48^s$	010600	1	12.58
PN G006.3+04.4	H 2-18	$17^h43^m34^s9$	$-21^d15^m44^s$	010600	0	44.04
PN G006.8−19.8	Wray 16-423	$19^h22^m01^s0$	$-31^d24^m57^s$	011600	0	44.04
PN G006.8+02.0	Pe 2-10	$17^h53^m43^s9$	$-22^d04^m33^s$	010600	0	44.04
PN G007.5+04.3	Th 4- 1	$17^h46^m26^s9$	$-20^d19^m41^s$	010600	0	44.04
PN G008.1−04.7	M 2-39	$18^h22^m09^s6$	$-24^d16^m24^s$	010600	0	12.58
PN G008.2−04.8	M 2-42	$18^h22^m40^s5$	$-24^d15^m13^s$	010600	0	12.58
PN G008.6−02.6	MaC 1-11	$18^h14^m58^s6$	$-22^d49^m42^s$	010600	0	44.04
PN G008.6−07.0	He 2-406	$18^h32^m01^s9$	$-24^d51^m58^s$	010600	0	12.58
PN G009.3+04.1	Th 4- 6	$17^h50^m57^s1$	$-18^d46^m47^s$	010600	1	12.58
PN G010.6+03.2	Th 4-10	$17^h57^m06^s5$	$-18^d06^m42^s$	010600	1	12.58
PN G011.1+07.0	Sa 2-237	$17^h44^m48^s2$	$-15^d51^m04^s$	010600	0	44.04
PN G011.3−09.4	H 2-48	$18^h46^m35^s0$	$-23^d26^m47^s$	010700	1	12.58
PN G011.7−06.6	M 1-55	$18^h36^m42^s5$	$-21^d48^m58^s$	010700	1	12.58
PN G012.5−09.8	M 1-62	$18^h50^m35^s5$	$-22^d40^m01^s$	010700	0	12.58
PN G 012.6−02.7	M 1-45	$18^h23^m15^s2$	$-19^d22^m54^s$	010600	0	12.58
PN G014.0−05.5	V-V 3-5	$18^h36^m40^s0$	$-19^d25^m14^s$	010600	0	12.58
PN G 014.3−05.5	V-V 3-6	$18^h37^m18^s8$	$-19^d08^m08^s$	010600	0	12.58
PN G016.9−02.0	Sa 3-134	$18^h29^m19^s7$	$-15^d07^m39^s$	010600	1	12.58
PN G018.6−02.2	M 3-54	$18^h33^m09^s9$	$-13^d50^m12^s$	010600	0	12.58
PN G019.2−02.2	M 4-10	$18^h34^m19^s9$	$-13^d18^m17^s$	010600	0	12.58
PN G 019.4−05.3	M 1-61	$18^h45^m55^s0$	$-14^d27^m37^s$	010700	1	12.58
PN G019.7+03.2	M 3-25	$18^h15^m16^s9$	$-10^d10^m08^s$	010600	1	12.58
PN G019.8+05.6	CTS 1	$18^h07^m04^s5$	$-09^d01^m29^s$	010600	0	44.04
PN G023.8−01.7	K 3-11	$18^h40^m58^s5$	$-08^d50^m20^s$	010300	0	12.58
PN G023.9+01.2	MA 13	$18^h30^m18^s5$	$-07^d22^m22^s$	010400	0	44.04
PN G025.3−04.6	K 4- 8	$18^h54^m29^s2$	$-08^d53^m10^s$	010700	0	12.58
PN G026.0−01.8	Pe 2-15	$18^h45^m36^s2$	$-07^d02^m37^s$	010700	0	44.04
PN G027.6−09.6	IC 4846	$19^h16^m16^s1$	$-08^d57^m21^s$	010400	0	12.58
PN G031.0+04.1	K 3- 6	$18^h33^m17^s6$	$+00^d11^m47^s$	010400	1	12.58
PN G032.5−03.2	K 3-20	$19^h01^m56^s8$	$-01^d43^m43^s$	011600	0	12.58
PN G032.9−02.8	K 3-19	$19^h01^m23^s3$	$-01^d14^m04^s$	010400	0	12.58
PN G034.0+02.2	K 3-13	$18^h45^m24^s7$	$+02^d01^m23^s$	010400	1	12.58
PN G038.4−03.3	K 4-19	$19^h13^m31^s4$	$+03^d19^m22^s$	010700	0	12.58
PN G038.7−03.3	M 1-69	$19^h14^m02^s7$	$+03^d32^m03^s$	010700	0	12.58
PN G041.8+04.4	K 3-15	$18^h51^m41^s6$	$+09^d54^m53^s$	011600	1	12.58
PN G042.0+05.4	K 3-14	$18^h48^m42^s1$	$+10^d30^m14^s$	010700	0	12.58
PN G042.9−06.9	NC 6807	$19^h34^m33^s4$	$+05^d41^m04^s$	010700	1	12.58
PN G044.1+05.8	CTSS 2	$18^h50^m55^s8$	$+12^d31^m52^s$	010700	0	44.04
PN G045.9−01.9	K 3-33	$19^h22^m26^s8$	$+10^d41^m21^s$	010400	1	12.58
PN G048.1+01.1	K 3-29	$19^h15^m30^s7$	$+14^d03^m49^s$	010400	1	12.58
PN G048.5+04.2	K 4-16	$19^h04^m35^s3$	$+15^d52^m16^s$	011600	0	12.58
PN G051.0+02.8	WhMe 1	$19^h14^m59^s9$	$+17^d22^m45^s$	010400	1	12.58
PN G052.9−02.7	K 3-41	$19^h39^m01^s1$	$+16^d25^m43^s$	010400	0	12.58
PN G 052.9+02.7	K 3-31	$19^h19^m02^s8$	$+19^d02^m20^s$	010400	1	12.58
PN G055.1−01.8	K 3-43	$19^h40^m10^s8$	$+18^d54^m07^s$	010400	0	12.58
PN G055.5−00.5	M 1-71	$19^h36^m27^s1$	$+19^d42^m23^s$	010400	1	12.58

Table 1
(Continued)

Name (1)	Alias (2)	α_{2000} (3)	δ_{2000} (4)	IRS Campaign (5)	Mode (6)	t_{exp} (s) (7)
PN G058.9+01.3	K 3-40	$19^h36^m09^s3$	$+23^d45^m08^s$	010400	0	12.58
PN G059.4+02.3	K 3-37	$19^h33^m34^s0$	$+24^d37^m46^s$	010400	0	12.58
PN G059.9+02.0	K 3-39	$19^h35^m54^s6$	$+24^d54^m48^s$	010400	1	12.58
PN G 060.5+01.8	He 2-440	$19^h38^m08^s5$	$+25^d15^m40^s$	010400	1	12.58
PN G063.8−03.3	K 3-54	$20^h04^m43^s6$	$+25^d31^m38^s$	010400	0	12.58
PN G067.9−00.2	K 3-52	$20^h03^m11^s6$	$+30^d32^m34^s$	010400	1	12.58
PN G068.7+01.9	K 4-41	$19^h56^m34^s2$	$+32^d22^m12^s$	010400	1	12.58
PN G068.7+14.8	Sp 4-1	$19^h00^m09^s2$	$+38^d26^m07^s$	010400	0	44.04
PN G069.2+02.8	K 3-49	$19^h54^m00^s8$	$+33^d22^m12^s$	010400	1	12.58
PN G077.7+03.1	Kj 2	$20^h15^m22^s4$	$+40^d34^m46^s$	009400	1	12.58
PN G 079.9+06.4	K 3-56	$20^h06^m21^s7$	$+44^d14^m40^s$	009400	0	12.58
PN G082.5+11.3	NC 6833	$19^h49^m12^s5$	$+48^d59^m60^s$	011400	0	44.04
PN G088.7+04.6	K 3-78	$20^h44^m45^s5$	$+50^d23^m52^s$	009400	0	12.58
PN G095.2+00.7	K 3-62	$21^h31^m50^s4$	$+52^d33^m52^s$	009400	1	12.58
PN G097.6−02.4	M 2-50	$21^h57^m06^s9$	$+51^d44^m22^s$	009400	0	12.58
PN G104.1+01.0	Bl 2- 1	$22^h20^m16^s7$	$+58^d14^m18^s$	010600	1	12.58
PN G107.4−00.6	K 4-57	$22^h48^m34^s5$	$+58^d29^m10^s$	010600	1	12.58
PN G107.4−02.6	K 3-87	$22^h54^m23^s6$	$+56^d43^m38^s$	009500	0	12.58
PN G112.5−00.1	Kj 8	$23^h23^m22^s8$	$+60^d59^m18^s$	009500	0	44.04
PN G184.0−02.1	M 1- 5	$05^h46^m50^s1$	$+24^d22^m01^s$	010700	1	12.58
PN G205.8−26.7	MaC 2- 1	$05^h03^m39^s7$	$−06^d04^m01^s$	010700	0	44.04
PN G235.3−03.9	M 1-12	$07^h19^m21^s6$	$−21^d43^m57^s$	010800	1	12.58
PN G263.0−05.5	PB 2	$08^h20^m52^s6$	$−46^d17^m19^s$	010900	0	12.58
PN G264.4−12.7	He 2- 5	$07^h47^m21^s5$	$−51^d09^m01^s$	010800	0	12.58
PN G274.1+02.5	He 2- 34	$09^h41^m13^s9$	$−49^d22^m46^s$	011400	1	12.58
PN G275.3−04.7	He 2- 21	$09^h14^m04^s7$	$−55^d22^m28^s$	011800	0	44.04
PN G278.6−06.7	He 2- 26	$09^h19^m44^s4$	$−59^d06^m22^s$	011900	0	12.58
PN G285.4+01.5	Pe 1- 1	$10^h38^m27^s6$	$−56^d47^m05^s$	009400	1	12.58
PN G285.4+02.2	Pe 2- 7	$10^h40^m56^s6$	$−56^d14^m24^s$	009400	0	12.58
PN G286.0−06.5	He 2- 41	$10^h07^m58^s9$	$−63^d49^m52^s$	011000	0	12.58
PN G289.8+07.7	He 2- 63	$11^h24^m17^s1$	$−52^d45^m47^s$	011000	0	44.04
PN G294.9−04.3	He 2- 68	$11^h31^m45^s9$	$−65^d58^m15^s$	011100	3	12.58
PN G295.3−09.3	He 2- 62	$11^h17^m14^s2$	$−70^d55^m06^s$	009400	0	12.58
PN G296.3−03.0	He 2- 73	$11^h48^m38^s7$	$−65^d08^m39^s$	011100	3	12.58
PN G297.4+03.7	He 2- 78	$12^h09^m24^s5$	$−58^d48^m23^s$	011400	0	12.58
PN G300.7−02.0	He 2- 86	$12^h30^m30^s5$	$−64^d52^m07^s$	012000	1	12.58
PN G307.5−04.9	MyCn 18	$13^h39^m34^s9$	$−67^d22^m50^s$	009400	1	12.58
PN G309.0+00.8	He 2- 96	$13^h42^m36^s0$	$−61^d22^m28^s$	009400	1	12.58
PN G309.5−02.9	MaC 1- 2	$13^h54^m37^s5$	$−65^d05^m33^s$	009400	0	44.04
PN G311.1+03.4	He 2-101	$13^h54^m55^s6$	$−58^d27^m15^s$	009400	1	12.58
PN G321.3+02.8	He 2-115	$15^h05^m16^s7$	$−55^d11^m09^s$	010600	1	12.58
PN G324.2+02.5	He 2-125	$15^h23^m33^s8$	$−53^d57^m30^s$	010600	0	12.58
PN G324.8−01.1	He 2-133	$15^h41^m58^s7$	$−56^d36^m24^s$	010600	1	12.58
PN G325.0+03.2	He 2-129	$15^h25^m41^s8$	$−52^d56^m32^s$	009500	0	12.58
PN G325.8−12.8	He 2-182	$16^h54^m35^s0$	$−64^d14^m27^s$	010600	1	12.58
PN G326.0−06.5	He 2-151	$16^h15^m42^s1$	$−59^d53^m60^s$	010600	1	12.58
PN G327.1−01.8	He 2-140	$15^h58^m08^s0$	$−55^d41^m49^s$	010600	1	12.58
PN G327.8−06.1	He 2-158	$16^h23^m36^s1$	$−58^d25^m23^s$	010600	0	12.58
PN G327.9−04.3	He 2-147	$16^h14^m00^s9$	$−56^d59^m26^s$	010600	1	12.58
PN G329.4−02.7	He 2-149	$16^h14^m27^s7$	$−54^d53^m41^s$	010600	0	12.58
PN G331.0−02.7	He 2-157	$16^h22^m14^s1$	$−53^d40^m53^s$	010600	1	12.58
PN G334.8−07.4	SaSt 2- 12	$17^h03^m13^s2$	$−54^d01^m46^s$	010600	0	12.58
PN G336.3−05.6	He 2-186	$16^h59^m45^s2$	$−51^d47^m59^s$	010600	0	12.58
PN G336.9+08.3	StWr 4-10	$16^h02^m14^s5$	$−41^d39^m39^s$	010600	0	12.58
PN G340.9−04.6	Sa 1-5	$17^h11^m36^s7$	$−47^d30^m52^s$	010600	0	12.58
PN G341.5−09.1	He 2-248	$17^h36^m16^s9$	$−49^d31^m35^s$	010600	0	44.04
PN G343.4+11.9	H 1- 1	$16^h13^m30^s6$	$−34^d41^m41^s$	010600	0	44.04
PN G344.2+04.7	Vd 1-1	$16^h42^m38^s4$	$−39^d00^m30^s$	010600	0	12.58
PN G344.4−06.1	Wray 16-278	$17^h30^m15^s0$	$−45^d28^m34^s$	010600	0	44.04
PN G344.4+02.8	Vd 1-5	$16^h51^m37^s8$	$−40^d08^m56^s$	010600	0	44.04
PN G344.8+03.4	Vd 1-3	$16^h49^m41^s9$	$−39^d26^m57^s$	009500	0	44.04
PN G345.0+04.3	Vd 1-2	$16^h46^m50^s6$	$−38^d42^m55^s$	010600	0	12.58
PN G348.4−04.1	H 1-21	$17^h32^m57^s7$	$−41^d04^m14^s$	010600	0	12.58
PN G348.8−09.0	He 2-306	$17^h56^m46^s2$	$−43^d08^m55^s$	010600	0	12.58
PN G350.8−02.4	H 1-22	$17^h32^m22^s0$	$−37^d57^m23^s$	010600	1	12.58

Table 1
(Continued)

Name (1)	Alias (2)	α_{2000} (3)	δ_{2000} (4)	IRS Campaign (5)	Mode (6)	t_{exp} (s) (7)
PN G351.3+07.6	H 1- 4	$16^h53^m41^s.4$	$-31^d46^m32^s$	010600	0	44.04
PN G351.9−01.9	Wray 16-286	$17^h33^m00^s.6$	$-36^d43^m51^s$	010600	1	12.58
PN G352.6+03.0	H 1- 8	$17^h14^m48^s.7$	$-33^d30^m43^s$	010600	0	44.04
PN G354.2+04.3	M 2-10	$17^h14^m13^s.4$	$-31^d25^m36^s$	010600	0	12.58
PN G354.9+03.5	Th 3- 6	$17^h19^m20^s.1$	$-31^d12^m39^s$	010600	1	12.58
PN G355.2−02.5	H 1-29	$17^h44^m13^s.7$	$-34^d17^m32^s$	010600	1	12.58
PN G355.7−03.0	H 1-33	$17^h47^m58^s.4$	$-34^d13^m51^s$	010600	0	44.04
PN G355.9+02.7	Th 3-10	$17^h24^m40^s.8$	$-30^d51^m58^s$	010600	1	12.58
PN G356.2−04.4	Cn 2-1	$17^h54^m32^s.9$	$-34^d22^m20^s$	010600	1	12.58
PN G356.5−03.6	H 2-27	$17^h51^m50^s.5$	$-33^d47^m35^s$	010600	1	12.58
PN G356.5+01.5	Th 3-55	$17^h30^m58^s.7$	$-31^d01^m05^s$	010600	1	12.58
PN G356.8+03.3	Th 3-12	$17^h25^m06^s.0$	$-29^d45^m16^s$	010600	1	12.58
PN G357.1−06.1	M 3-50	$18^h04^m15^s.4$	$-34^d34^m18^s$	010600	0	44.04
PN G357.1+01.9	Th 3-24	$17^h30^m57^s.9$	$-30^d23^m05^s$	010600	0	44.04
PN G357.2+02.0	H 2-13	$17^h31^m14^s.6$	$-30^d16^m21^s$	010600	0	44.04
PN G357.6+01.7	H 1-23	$17^h32^m47^s.0$	$-30^d00^m16^s$	010600	1	12.58
PN G357.6+02.6	H 1-18	$17^h29^m42^s.7$	$-29^d32^m49^s$	010600	1	12.58
PN G358.2+03.6	M 3-10	$17^h27^m20^s.1$	$-28^d27^m50^s$	010600	1	12.58
PN G358.3+01.2	Bl B	$17^h37^m06^s.7$	$-29^d46^m01^s$	010600	0	44.04
PN G358.5−04.2	H 1-46	$17^h59^m02^s.4$	$-32^d21^m42^s$	010600	1	12.58
PN G358.5+02.9	Al 2-F	$17^h30^m36^s.8$	$-28^d41^m48^s$	010600	0	44.04
PN G358.6+01.8	M 4- 6	$17^h35^m13^s.9$	$-29^d03^m09^s$	010600	1	12.58
PN G358.7−02.7	Al 2-R	$17^h53^m45^s.1$	$-31^d31^m11^s$	010600	0	44.04
PN G358.7+05.2	M 3-40	$17^h22^m28^s.2$	$-27^d08^m41^s$	010600	1	12.58
PN G358.9−03.7	H 1-44	$17^h58^m10^s.5$	$-31^d42^m55^s$	010600	1	12.58
PN G358.9+03.4	H 1-19	$17^h30^m02^s.5$	$-27^d59^m16^s$	010600	1	12.58
PN G359.3+03.6	Al 2-E	$17^h30^m14^s.3$	$-27^d30^m18^s$	010600	1	12.58
PN G359.4+02.3	Th 3-32	$17^h35^m22^s.1$	$-28^d12^m54^s$	010600	0	44.04

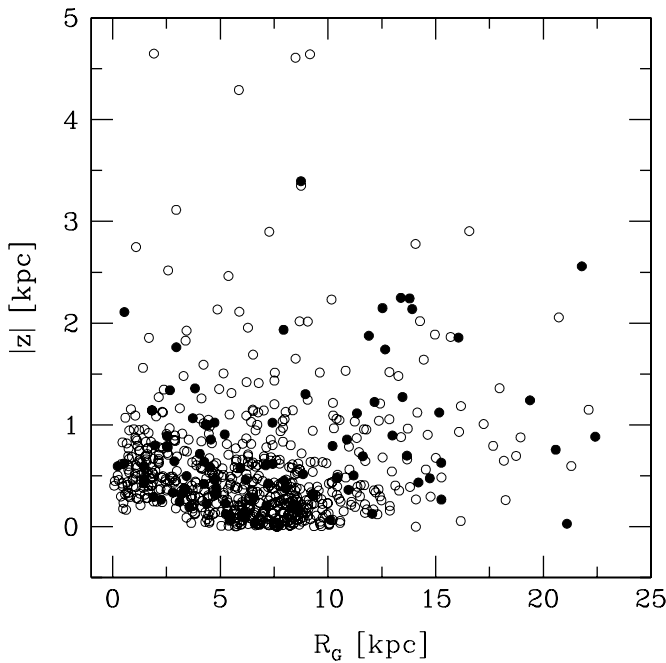(This table is also available in a machine-readable form in the online journal.)

Figure 1. Spatial distribution of our targets (filled circles) compared to the general PN population in the Galaxy (open circles). This plot is limited to those PNe whose statistical distance could be calculated, thus it represents subsamples of both our target sample and the general Galactic PN population.

exposure time and the number of cycles needed for each mode using *Spitzer* IRS Performance Estimator Tool, the saturation levels for all modes, and a conservative choice for the fluxes.

For the PN with very low fluxes, based on the *IRAS* upper limits and our experience with IRS spectra of Magellanic Cloud PN, we observed in SL and LL modes, with three integrations of, respectively, 14 and 30 s each. Peak up observations were not necessary, since we derive all coordinates from the astrometric catalog by Kerber et al. (2003), where the precision is better than 0''.35.

3. DATA ANALYSIS: CALIBRATION, SPECTRAL EXTRACTION, AND DUST CLASSIFICATION

Raw data were retrieved from the *Spitzer* archive together with the latest pipeline calibration files. Initial file preparation included removing *Bowing* of spectral orders in the LH data using DARK SETTLE; cleaning rogue pixels using IRSCLEAN MASK, where we used custom masks for rogue pixels cleaning for all our data; and subtracting the two nod positions for the SL and LL data to obtain sky-subtracted spectra. All low-resolution spectral images were checked free from background source contamination. We did not subtract the sky in the high-resolution data, but the sky background is very low for these bright sources. We then extracted the one-dimensional spectra from the co-added two-dimensional spectral images using SPICE version 2.2.

The spectral merging, averaging, and continuum fitting was done with the package SMART (Higdon et al. 2004). The final spectrum for each data set includes merging, cleaning and subtracting any spurious jump, and averaging the nod positions and orders. We subtracted a spurious pedestal above $14\,\mu m$ from the spectrum of PN G012.5−09.8, so both final reduced

spectrum and the fitted blackbody curve have been modified accordingly. We also subtracted a pedestal along the whole spectrum of PN G041.8+04.4 and PN G044.1+05.8 to bring it down to a level of 0.0 Jy at $5\,\mu$m.

Three distinct components are apparent in the spectral energy distributions (SEDs): the dust continuum, the nebular emission in the form of collisionally excited lines of atomic gas, and, in the majority of the targets, solid-state dust emission features. An analysis of the abundances in the nebular atomic gas will be presented in a future paper; for now, we focus on the spectral signatures of the dust. We fit the dust continuum in each target with the blackbody-fitting routine described in the package SMART/IDEA in order to determine a characteristic dust temperature and IR luminosity. We performed a continuum fit on each spectrum after masking the nebular and solid-state emission features and the low-signal region longward of $\sim 37\,\mu$m where the system sensitivity drops rapidly. The temperature and luminosity were varied to minimize the rms deviation, and the IR luminosity was derived from the integral of the Planck function at that temperature over all wavelengths. In most cases, the continuum was well sampled over the bulk of the observed spectrum, through the whole SED, and we constrained the fitted function to pass through or below the average continuum.

The form of the fitting included an emissivity term, $\tau \propto \lambda^{-\alpha}$ (α is given in Column 5 of Table 3 for the converging fits), and the fitting routine finds a solution for both alpha and the proportionality constant (see also Hony et al. 2002). The blackbody fits were robustly obtained for about half of the PN sample, and in these cases the formal uncertainties of the fit to temperature and IR luminosity were small, owing to the very slow change in the Planck function with wavelength. For cases where the fits did not converge with the proposed method (flagged as *N* in Table 3, Column 4), we did not use the derived dust temperatures in the tables or figures of this paper. We plan to use more sophisticated fitting models in a future analysis. For the PNe whose blackbody fits converge, we have validated them further by comparing the fits against the $65\,\mu$m fluxes from the Akari data archive, and the $60\,\mu$m fluxes from *IRAS* archive[10] in order to determine whether the IRS spectra do sample their flux maxima (i.e., the 60 [or 65] μm flux is lower than the maximum flux of the IRS spectra). In these cases, we also have checked whether the 60–65 μm fluxes in the literature were not lower than our continuum fit extrapolations at the same wavelength. The majority of the (converging) fitted continua are perfectly compatible with the long-wavelength photometry where available (55 PNe, flagged with *A* in Table 3, Column 4); the IR flux longward of $60\,\mu$m shows that the observed SEDs sample the functional maximum of the fits. Furthermore, our extrapolated fluxes and those in the literature correlate very well with one another, with a global (linear) correlation coefficient of 0.82. We use the *A* fits with confidence in our group analysis and figures.

Another 14 PNe are below the limit of detectability of the Akari and *IRAS* satellites at 60–65 μm, although their continuum fits seem to be excellent; they are flagged with *B* in Column 4 of Table 3.

---

[10] In Table 3, Column 6, we give the satellite fluxes we have used to asses the validity of the fits, where we used the Akari 65 μm flux (Yamamura et al. 2010) when available, otherwise the 60 μm *IRAS* flux (given in Acker et al. 1992). Errors are given when available from the Akari data archives; flux errors are not available for *IRAS*, only flux quality, where a low quality indicates an upper limit to the 60 μm flux, which is still valid, in our case, to constraint the continuum fit.

Table 2
Classification Scheme

Class (1)	Description (2)	Subclass (3)	$N_{\rm PN}$ (4)
F	Dust continuum		25 (17%)
CRD	Carbon-rich dust		38 (25%)
		Aromatic	13
		Aliphatic	22
		Aromatic/aliphatic	3
ORD	Oxygen-rich dust		45 (30%)
		Crystalline	16
		Amorphous	24
		Crystalline/amorphous	1
MCD	Mixed-chemistry dust		42 (28%)

Finally, 10 PNe have (converging) blackbody fits which are badly constrained by the 60–65 μm archival flux (they are flagged with *C* in Table 3, Column 4). What happens in these cases is that the 60 and/or 65 μm fluxes are considerably higher than the IRS flux maxima. This discrepancy can have several causes, including (a) a bad fit of the continuum, (2) the presence of other sources, or (3) high background at 60–65 μm. We have inspected these sources and found four possible bulge PNe among them, which could imply higher than average background, and one PN (PN G356.5−03.6) whose WISE data archive inspection within the *Spitzer* beam disclosed multiple sources which could cause the mismatch between the extrapolated fits and the 60–65 μm archival fluxes. For the remaining PNe, there is not a good explanation for the flux mismatch, likely an unexplained high background at long wavelength, and they will be studied in more detail in the future. To be very conservative with our conclusions, we will not use the blackbody fits that do not comply with the available 60–65 μm photometry in Figures 9–16 or the analysis (Section 4) of this paper.

While these blackbody fits reflect the physical origin of the continuum shape, this characterization is only broadly representative of the thermal dust. Indeed, the dust within a given nebula may be composed of a variety of chemical species, each with their own emissivity, at varying distances from the source of excitation. Thus, there may in reality be an ensemble of thermal emission within the nebula which is not perfectly represented by a single blackbody temperature. We revisit this point and the impact it could have on the analysis presented in Section 4.2. In addition, the residuals in the blackbody-subtracted continuum may complicate the interpretation of very broad, weak, solid-state features. For those, one needs to perform polynomial fits and subtractions (see, for example, García-Hernández et al. 2010).

In Table 2, we give a description of our dust classification scheme. We define therein the dust classes, and also several subclasses that we encounter in the analysis of our large sample of compact Galactic PNe. As for the Magellanic Cloud sample, we classify the spectra based on their dust features. A detailed analysis of the atomic emission lines and elemental abundances will be published elsewhere. We distinguish among (1) the absence of prominent dust features, (2) the presence of carbon-rich dust features, and (3) the presence of oxygen-rich dust features. PNe lacking prominent molecular/dust emission features and with very low continuum are defined as *F*. Those with carbon-rich features are in the *CRD* class, with subclasses determining weather they show aromatic and/or aliphatic features.
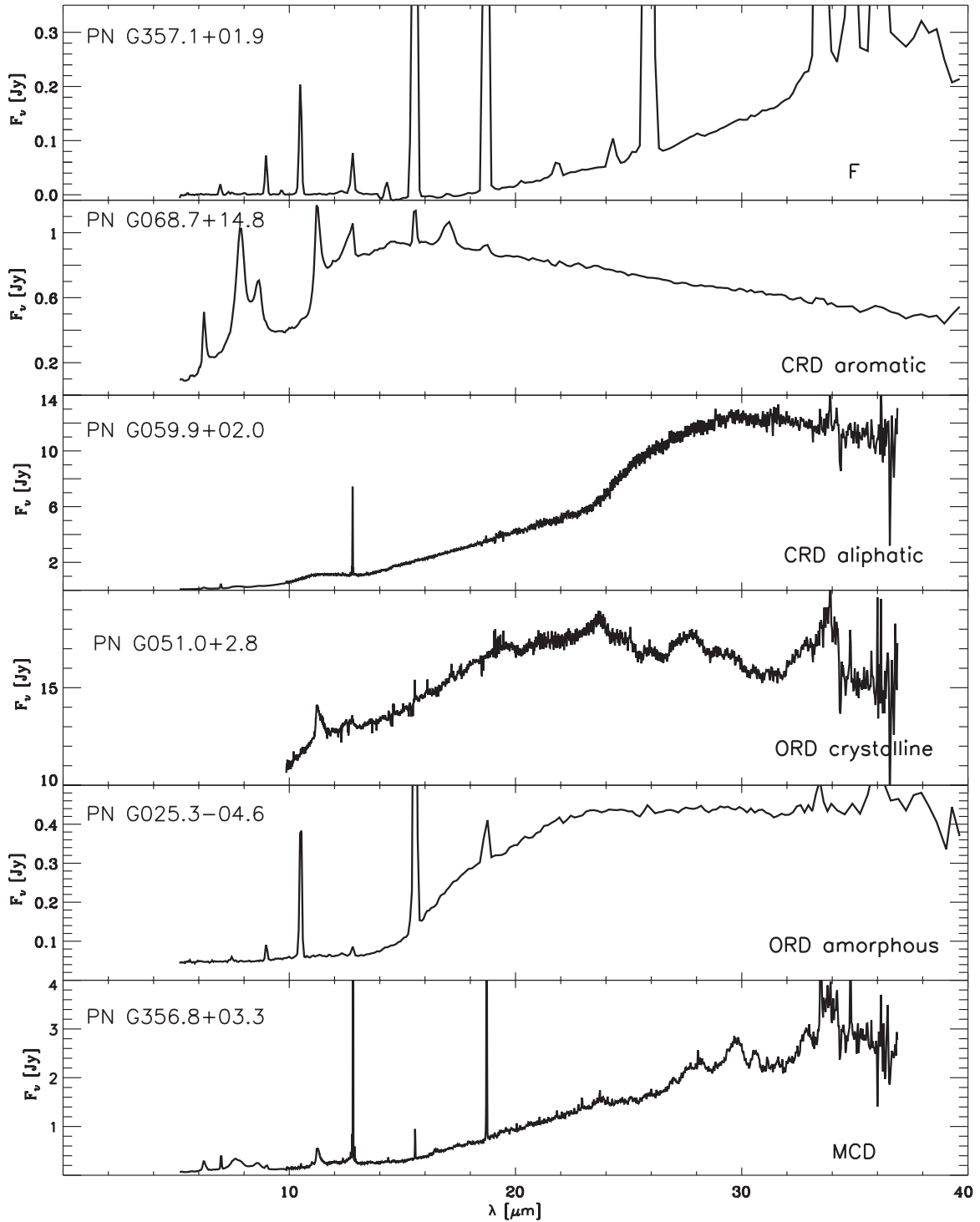
Figure 2. Spectral templates of dust types found in our compact Galactic PN sample.

This is similar for the oxygen-rich dust features, or *ORD*, where the subclasses indicate the presence of crystalline and/or amorphous dust grains. Finally, in many cases the spectra show both CRD and ORD characteristics, and we call these dual-chemistry PNe as *MCD* (or mixed-chemistry dust) PNe. In Figure 2, we present the array of template spectra according to dust class and subclass. Table 3 lists, for all targets, the dust class (Column 2) and subclass (Column 3).

In Figures 3–6, we plot all IRS PN spectra from our program, and we overplot (as dotted lines) the continuum fits for *A*

and *B* fit types (see Table 3). There are a total of 25 PNe with continuum-only (F) spectra; one is shown in Figure 2 (top panel), and the remaining 24 in Figure 3. None of these spectra shows very obvious molecular/dust emission features above the continuum, and the continua are very faint. In a couple of cases (PN G038.4−0.3. and PN G038.7−03.3, both in Figure 3), the dust profile has a different shape than the other F PNe, in particular there is a suggestion of a bump in the ~20–30 μm spectral region, thus the F designation might be uncertain. Actually, there may be some ORD or CRD PNe

Table 3
Dust Classification and Dust Parameters

Name	Class	Sub.[a]	Fit[c]	α	$F_{\rm ref.}$ (Jy)	$T_{\rm dust}$ (K)	$\log L_{\rm IR}$ ($L_\odot$)	IRE
(1)	(2)	(3)	(4)	(5)	(6)	(7)	(8)	(9)
PN G000.3−02.8	F	0	B	1.02	. . .	65.81 ± 2.58	. . .	. . .
PN G000.6−01.3	CRD	3	N	. . .	. . .	. . .	. . .	. . .
PN G000.6−02.3	MCD	7	N	. . .	. . .	. . .	. . .	. . .
PN G000.8−01.5	MCD	7	A	2.20	4.77[d]	79.38 ± 1.80	. . .	. . .
PN G000.8−07.6	CRD	1[b]	N	. . .	. . .	. . .	. . .	. . .
PN G001.7−01.6	MCD	7	B	2.58	. . .	76.23 ± 5.56	. . .	. . .
PN G001.7−04.6	ORD	4	A	2.22	1.41[e]	82.31 ± 1.76	2.920	2.920
PN G002.4−03.7	MCD	7	A	2.79	5.21[d]	77.05 ± 0.90	2.837	2.837
PN G002.6−03.4	MCD	7	A	2.68	9.19[d]	75.74 ± 0.88	. . .	. . .
PN G002.9−03.9	ORD	5[b]	N	. . .	. . .	. . .	. . .	. . .
PN G003.0−02.6	CRD	2[b]	N	. . .	. . .	. . .	. . .	. . .
PN G003.1+03.4	MCD	7	A	1.95[d]	3.92 ± 0.49[e]	79.12 ± 1.83	3.064	3.064
PN G003.2−04.4	ORD	5[b]	B	2.39	. . .	77.88 ± 3.31	2.346	2.346
PN G003.9−14.9	ORD	5[b]	A	5.52	1.93	70.27 ± 2.00	2.714	2.714
PN G004.1−03.8	ORD	5[b]	B	0.00	. . .	126.00 ± 4.55	1.768	1.768
PN G004.3−02.6	MCD	7	N	. . .	. . .	. . .	. . .	. . .
PN G004.9−04.9	MCD	7	C	0.16	5.19	98.87 ± 3.18	2.669	2.669
PN G005.5+0.27	MCD	7	C	6.63	13.30[d]	57.07 ± 1.13	. . .	. . .
PN G006.0+02.8	MCD	7	A	6.38	1.11[e]	58.13 ± 0.74	. . .	. . .
PN G006.3+04.4	ORD	5[b]	N	. . .	. . .	. . .	. . .	. . .
PN G006.8+02.0	MCD	7	N	. . .	. . .	. . .	. . .	. . .
PN G006.8−19.8	CRD	3	N	. . .	. . .	. . .	. . .	. . .
PN G007.5+04.3	ORD	4	N	. . .	. . .	. . .	. . .	. . .
PN G008.1−04.7	ORD	4	N	. . .	. . .	. . .	. . .	. . .
PN G008.2−04.8	F	0	N	. . .	. . .	. . .	. . .	. . .
PN G008.6−02.6	ORD	5	N	. . .	. . .	. . .	. . .	. . .
PN G008.6−07.0	F	0	N	. . .	. . .	. . .	. . .	. . .
PN G009.3+04.1	ORD	6[b]	C	2.19	0.85[d]	87.89 ± 1.40	. . .	. . .
PN G010.6+03.2	CRD	1	A	1.58	1.82[e]	91.72 ± 2.19	. . .	. . .
PN G011.1+07.0	ORD	5	N	. . .	. . .	. . .	. . .	. . .
PN G011.3−09.4	ORD	5	N	. . .	. . .	. . .	. . .	. . .
PN G011.7−06.6	NA	8	N	. . .	. . .	. . .	. . .	. . .
PN G012.5−09.8	CRD	2[b]	N	. . .	. . .	. . .	. . .	. . .
PN G012.6−02.7	MCD	7	N	. . .	. . .	. . .	. . .	. . .
PN G014.0−05.5	F	0	C	1.34	1.91 ± 0.58[e]	77.46 ± 3.42	. . .	. . .
PN G014.3−05.5	CRD	1	N	. . .	. . .	. . .	. . .	. . .
PN G016.9−02.0	MCD	7	N	. . .	. . .	. . .	. . .	. . .
PN G018.6−02.2	F	0	N	. . .	. . .	. . .	. . .	. . .
PN G019.2−02.2	ORD	6	B	3.28	. . .	75.58 ± 4.54	2.915	2.915
PN G019.4−05.3	MCD	7	N	. . .	. . .	. . .	. . .	. . .
PN G019.7+03.2	MCD	7	A	1.00	10.37 ± 2.18[e]	102.40 ± 5.36	3.242	3.242
PN G019.8+05.6	F	0	N	. . .	. . .	. . .	. . .	. . .
PN G023.8−01.7	MCD	7	A	3.36	8.77 ± 2.11[e]	74.76 ± 1.83	3.377	3.377
PN G023.9+01.2	MCD	7	A	2.85	10.93 ± 1.70[e]	76.23 ± 1.49	. . .	. . .
PN G025.3−04.6	ORD	5	N	. . .	. . .	. . .	. . .	. . .
PN G026.0−01.8	ORD	5[b]	N	. . .	. . .	. . .	. . .	. . .
PN G027.6−09.6	ORD	5	N	. . .	. . .	. . .	. . .	. . .
PN G031.0+04.1	ORD	4	A	4.12	5.50 ± 0.54[e]	85.20 ± 2.53	3.218	3.218
PN G032.5−03.2	MCD	7	A	0.88	1.36[e]	104.20 ± 6.46	. . .	. . .
PN G032.9−02.8	CRD	2	A	0.00	2.56[d]	146.80 ± 7.62	3.000	3.000
PN G034.0+02.2	ORD	4	A	0.92	3.56[d]	88.48 ± 1.87	2.699	2.699
PN G038.4−03.3	F	0	A	1.62	2.14 ± 0.01[e]	84.15 ± 3.54	. . .	. . .
PN G038.7−03.3	F	0	A	2.11	3.23 ± 0.73[e]	80.52 ± 3.25	. . .	. . .
PN G041.8+04.4	CRD	3	A	1.50	0.52[e]	127.20 ± 5.24	. . .	. . .
PN G042.0+05.4	ORD	5	N	. . .	. . .	. . .	. . .	. . .
PN G042.9−06.9	ORD	6	A	7.16	0.65[e]	63.87 ± 0.66	3.703	3.703
PN G044.1+05.8	NA	8	N	. . .	. . .	. . .	. . .	. . .
PN G045.9−01.9	MCD	7	A	2.98	3.46[d]	77.65 ± 0.79	3.394	3.394
PN G048.1+01.1	CRD	1	N	. . .	. . .	. . .	. . .	. . .
PN G048.5+04.2	CRD	2[b]	B	0.00	. . .	108.20 ± 3.60	2.153	2.153
PN G051.0+02.8	ORD	4	A	0.00	6.39 ± 0.54[e]	224.60 ± 12.59	. . .	. . .
PN G052.9+02.7	CRD	2	N	. . .	. . .	. . .	. . .	. . .
PN G052.9−02.7	F	0	N	. . .	. . .	. . .	. . .	. . .
PN G055.1−01.8	F	0	N	. . .	. . .	. . .	. . .	. . .

Table 3
(Continued)

Name	Class	Sub.[a]	Fit[c]	α	$F_{\rm ref.}$ (Jy)	$T_{\rm dust}$ (K)	$\log L_{\rm IR}$ ($L_\odot$)	IRE
(1)	(2)	(3)	(4)	(5)	(6)	(7)	(8)	(9)
PN G055.5−00.5	CRD	2	N	...	...	...	...	...
PN G058.9+01.3	ORD	4	N	...	...	...	...	...
PN G059.4+02.3	CRD	2	A	0.00	0.80[e]	124.00 ± 4.89	2.512	2.512
PN G059.9+02.0	CRD	2	N	...	...	...	...	...
PN G060.5+01.8	ORD	4	A	2.31	2.70 ± 0.16[e]	85.94 ± 2.01	3.297	3.297
PN G063.8−03.3	CRD	2	N	...	...	...	...	...
PN G067.9−00.2	ORD	4	C	0.00	35.94 ± 2.70[e]	124.50 ± 1.93	3.164	3.164
PN G068.7+01.9	ORD	4	A	1.46	2.44 ± 0.10[e]	86.26 ± 1.71	2.805	2.805
PN G068.7+14.8	CRD	1	N	...	...	...	...	...
PN G069.2+02.8	ORD	5	A	3.03	1.10 ± 0.36[e]	81.28 ± 2.89	3.351	3.351
PN G077.7+03.1	F	0	N	...	...	...	...	...
PN G079.9+06.4	ORD	5[b]	B	0.70	...	118.00 ± 4.39	...	...
PN G082.5+11.3	F	0	N	...	...	...	...	...
PN G088.7+04.6	F	0	A	1.59	1.99 ± 0.36[e]	84.24 ± 3.63	2.550	2.550
PN G095.2+00.7	CRD	2	N	...	...	...	...	...
PN G097.6−02.4	ORD	5[b]	N	...	...	...	...	...
PN G104.1+01.0	CRD	1	A	0.00	2.66 ± 0.10[e]	157.70 ± 3.83	3.114	3.114
PN G107.4−00.6	NA	8	N	...	...	...	...	...
PN G107.4−02.6	CRD	2[b]	N	...	...	...	...	...
PN G112.5−00.1	F	0	N	...	...	...	...	...
PN G184.0−02.1	CRD	2	N	...	...	...	...	...
PN G205.8−26.7	CRD	2	B	1.02	...	122.30 ± 13.89	...	...
PN G235.3−03.9	CRD	2	N	...	...	...	...	
PN G263.0−05.5	CRD	2	N	...	...	...	...	
PN G264.4−12.7	CRD	2	N	...	...	...	...	...
PN G274.1+02.5	NA	8	N	...	...	...	...	...
PN G275.3−04.7	CRD	2	N	...	...	...	...	...
PN G278.6−06.7	CRD	2	A	0.53	1.52[d]	128.10 ± 13.15	2.815	2.815
PN G285.4+01.5	CRD	1	N	...	...	...	...	...
PN G285.4+02.2	F	0	N	...	...	...	...	...
PN G286.0−06.5	CRD	2	A	0.00	0.57[d]	143.80 ± 8.65	2.750	2.750
PN G289.8+07.7	F	0	B	0.00	...	128.80 ± 5.31	1.743	1.743
PN G294.9−04.3	CRD	2	N	...	...	...	...	...
PN G295.3−09.3	ORD	5	A	1.78	0.87[d]	97.33 ± 7.08	...	...
PN G296.3−03.0	MCD	7	A	2.27	5.00 ± 0.43[e]	82.11 ± 2.26	3.063	3.063
PN G297.4+03.7	CRD	1	N	...	...	...	...	...
PN G300.7−02.0	MCD	7	A	3.65	18.48 ± 1.11[e]	71.93 ± 1.62	3.450	3.450
PN G307.5−04.9	MCD	7	A	2.42	17.17 ± 0.78[e]	87.02 ± 1.20	2.834	2.834
PN G309.0+00.8	MCD	7	C	2.07	18.27 ± 1.43[e]	90.02 ± 2.37	...	...
PN G309.5−02.9	CRD	1[b]	N	...	...	...	...	...
PN G311.1+03.4	NA	8	N	...	...	...	...	...
PN G321.3+02.8	CRD	2	N	...	...	...	...	...
PN G324.2+02.5	MCD	7	A	3.26	2.86 ± 0.56[e]	70.53 ± 4.14	3.167	3.167
PN G324.8−01.1	MCD	7	A	3.12	19.45 ± 2.31	76.59 ± 1.67	3.125	3.125
PN G325.0+03.2	ORD	5	A	0.98	1.33[e]	99.32 ± 6.09	2.868	2.868
PN G325.8−12.8	ORD	5	A	5.63	0.72[e]	65.55 ± 0.59	2.496	2.496
PN G326.0−06.5	ORD	5	A	7.46	4.70 ± 0.93[e]	57.45 ± 0.39	3.560	3.560
PN G327.1−01.8	MCD	7	A	3.12	11.77 ± 3.41[e]	73.83 ± 1.28	3.318	3.318
PN G327.8−06.1	MCD	7	A	0.68	1.12[e]	103.90 ± 6.45	3.022	3.022
PN G327.9−04.3	NA	8	N	...	...	...	...	...
PN G329.4−02.7	F	0	N	...	...	...	...	...
PN G331.0−02.7	ORD	4	A	3.26	2.61[e]	75.65 ± 1.59	3.068	3.068
PN G334.8−07.4	ORD	4	A	0.81	0.41[d]	133.10 ± 10.75	...	...
PN G336.3−05.6	CRD	1	N	...	...	...	...	...
PN G336.9+08.3	ORD	5	N	...	...	...	...	...
PN G340.9−04.6	F	0	N	...	...	...	...	...
PN G341.5−09.1	F	0	N	...	...	...	...	...
PN G343.4+11.9	ORD	5	B	1.28	...	97.56 ± 14.71	2.301	2.301
PN G344.2+04.7	ORD	5	N	...	...	...	...	...
PN G344.4+02.8	CRD	2[b]	N	...	...	...	...	...
PN G344.8+03.4	CRD	1	N	...	...	...	...	...
PN G345.0+04.3	ORD	5	A	4.62	0.74[e]	69.58 ± 3.29	...	...
PN G348.4−04.1	MCD	7	N	...	...	...	...	...
PN G348.8−09.0	F	0	A	1.53	2.16[e]	88.05 ± 2.17	...	...

Table 3
(Continued)

Name	Class	Sub.[a]	Fit[c]	α	$F_{\text{ref.}}$ (Jy)	T_{dust} (K)	$\log L_{\text{IR}}$ ($L_\odot$)	IRE
(1)	(2)	(3)	(4)	(5)	(6)	(7)	(8)	(9)
PN G350.8−02.4	ORD	4	A	2.74	1.60[e]	72.27 ± 1.24	. . .	. . .
PN G351.3+07.6	ORD	5	N	. . .	. . .	. . .	. . .	. . .
PN G351.9−01.9	MCD	7	N	. . .	. . .	. . .	. . .	. . .
PN G352.6+03.0	MCD	7	B	2.38	. . .	77.00 ± 5.25	2.988	2.988
PN G354.2+04.3	CRD	1	N	. . .	. . .	. . .	. . .	. . .
PN G354.9+03.5	MCD	7	N	. . .	. . .	. . .	. . .	. . .
PN G355.2−02.5	MCD	7	A	0.22	1.53[d]	124.30 ± 4.33	2.059	2.059
PN G355.7−03.0	CRD	1	B	1.08	. . .	97.23 ± 6.07	2.770	2.770
PN G355.9+02.7	MCD	7	C	0.70	7.81 ± 2.33[e]	96.69 ± 5.66	3.179	3.179
PN G356.2−04.4	ORD	6	A	4.17	2.98 ± 0.14[e]	74.39 ± 1.81	3.062	3.062
PN G356.5+01.5	ORD	4	C	1.28	7.21[d]	88.89 ± 1.78	2.446	2.446
PN G356.5−03.6	F	0	C	0.46	2.03[e]	92.95 ± 1.27	. . .	. . .
PN G356.8+03.3	MCD	7	N	. . .	. . .	. . .	. . .	. . .
PN G357.1+01.9	F	0	N	. . .	. . .	. . .	. . .	. . .
PN G357.1−06.1	F	0	N	. . .	. . .	. . .	. . .	. . .
PN G357.2+02.0	MCD	7[b]	B	0.19	. . .	118.70 ± 7.02	. . .	. . .
PN G357.6+01.7	ORD	4	A	2.29	5.35[e]	83.75 ± 2.01	3.153	3.153
PN G357.6+02.6	MCD	7	A	1.86	6.59[d]	86.34 ± 2.49	2.026	2.026
PN G358.2+03.6	ORD	4	A	2.08	2.65[e]	89.06 ± 2.60	3.116	3.116
PN G358.3+01.2	MCD	7	N	. . .	. . .	. . .	. . .	. . .
PN G358.5+02.9	F	0	B	0.97	. . .	110.80 ± 5.39	. . .	. . .
PN G358.5−04.2	ORD	6	A	3.86	2.17 ± 0.35[e]	75.65 ± 1.61	1.616	1.616
PN G358.6+01.8	MCD	7	A	1.91[d]	4.28	90.02 ± 2.42	. . .	. . .
PN G358.7+05.2	MCD	7	C	. . .	. . .	73.37 ± 1.94	. . .	. . .
PN G358.7−02.7	NA	8	N	. . .	. . .	. . .	. . .	. . .
PN G358.9+03.4	MCD	7	A	2.52	5.17 ± 1.02[e]	79.98 ± 1.93	2.761	2.761
PN G358.9−03.7	MCD	7	N	. . .	. . .	. . .	. . .	. . .
PN G359.3+03.6	F	0	A	0.99	1.23[e]	86.01 ± 1.79	. . .	. . .
PN G359.4+02.3	MCD	7	A	2.14	3.98[e]	85.92 ± 3.75	. . .	. . .

Notes.

[a] Subclasses: 0 = featureless, 1 = aromatic, 2 = aliphatic, 3 = aromatic/aliphatic, 4 = crystalline, 5 = amorphous, 6 = crystalline/amorphous, 7 = MCD, 8 = other.

[b] Class or subclass uncertain.

[c] Blackbody fit. N = not converging (or, not a PN); A = good fit, excellent F_{ref} (60 or 65 μm) constraints; B = good fit, no constraints available; C = good fit, poor constraints (not used in the plots).

[d] $F_{\text{ref}} = F_{60\,\mu\text{m}}$ from *IRAS*.

[e] $F_{\text{ref}} = F_{65\,\mu\text{m}}$ from Akari.

(This table is also available in a machine-readable form in the online journal.)

among the subsample of objects with featureless spectra, but the weakness of the dust features prevents to confirm the dominant chemistry (ORD or CRD) of their circumstellar shells. It is worth noting that two of the F spectra (PN G356.5−03.6 and PN G359.3+03.6, both in Figure 3) show a jump between the SH and LH modules ($\sim\lambda < 19.5\,\mu$m) that, in principle, may be attributed to an extended nature of these sources at longer wavelengths. However, due to the compact nature ($<4''$) of our PN sample and because we do not see any mismatch between the SL and SH modules, we suspect that this LH flux excess is possibly due to a known systematic effect that may affect some LH observations (see, e.g., García-Hernández et al. 2007b) or, less likely, to background emission. In general, the background is very faint relative to the source in these LH observations, but there is really no way to check if this is indeed the case. In any case, this slight mismatch between the SH and LH observations does not affect any of our results. In these cases, we have scaled the continuum for the final fits.

Carbon-rich dust features can be aromatic or aliphatic. The aromatic features are represented by the well-known family of infrared features at 6.2, 7.7, 8.6, and 11.2 μm usually attributed to polycyclic aromatic hydrocarbons (PAHs; e.g., Leger & Puget 1984), or, as more appropriately defined by Kwok & Zhang (2011), to aromatic infrared bands (heretofore AIBs). The AIBs have been observed in several types of astronomical sources. It is worth noting that in several cases a single (and usually very weak) 11.2 μm feature in the spectra, especially if the feature is narrower than common AIB features, is due to interstellar rather than circumstellar emission, thus the nebula would not be classified as CRD solely on this emission feature. In Figure 2, we show a typical example of obvious AIB features in PN G068.7+14.8, where all four bands are clearly present. PNe with spectra showing any of these bands are classified as CRD; our sample includes 12 additional such spectra.

A larger number of the CRD spectra show other emission features that are likely related to carbon-rich dust as well, but of different types. The 6–9 μm feature can be attributed to hydrogenated amorphous carbons (HACs), large PAH clusters, or very small carbon grains. On the other hand, the broad 10–15 μm emission (centered at about 11.5 μm) and the 25–35 μm emission (the so-called 30 μm feature) are usually attributed to SiC (e.g., Speck et al. 2009) and MgS (e.g., Hony et al. 2002),
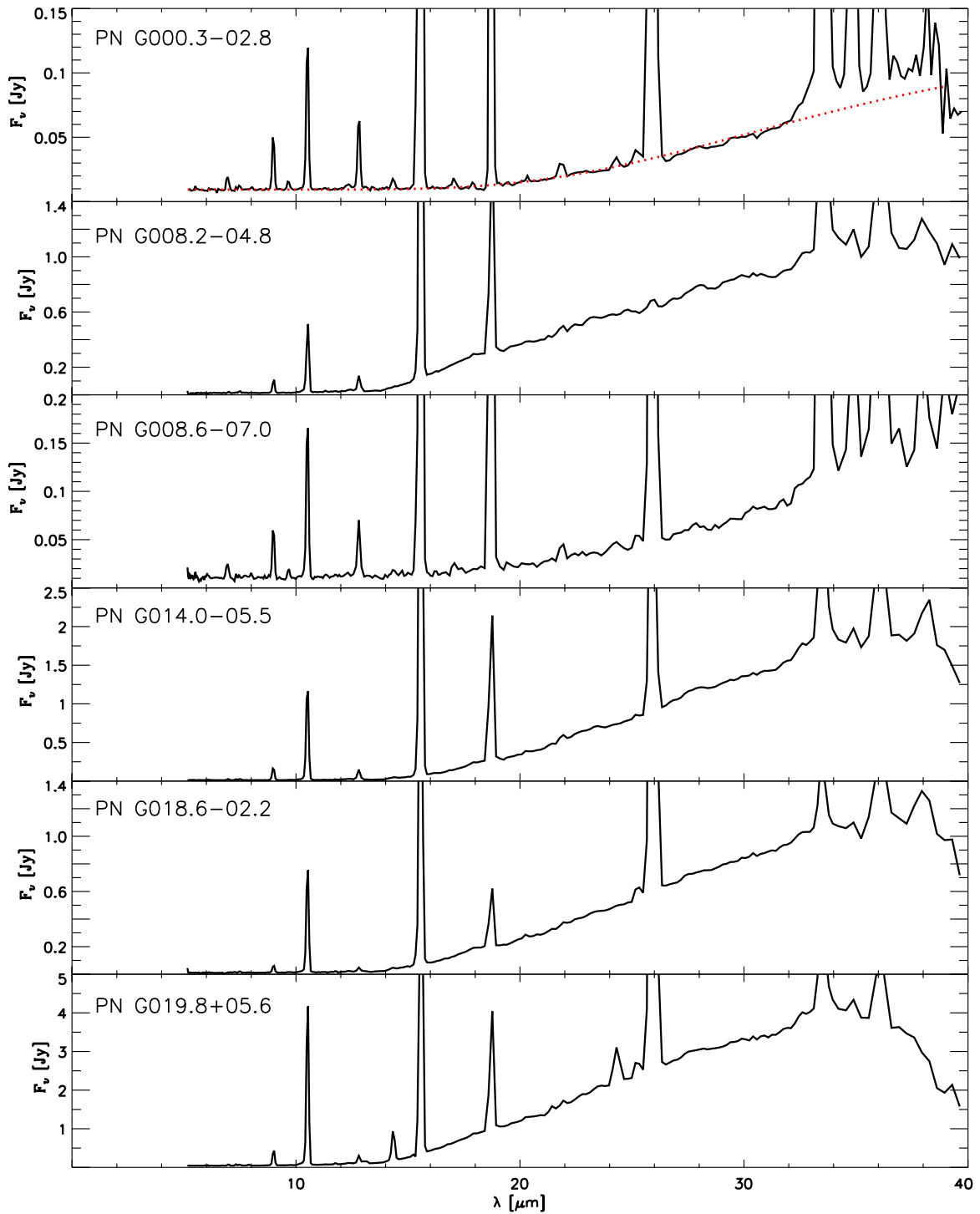
Figure 3. Featureless spectra, in PN G order. Dotted lines correspond to blackbody continuum fits of type *A* or *B* (see the text, and Table 3).

(An extended, color version of this figure is available in the online journal.)

respectively. However, the observed variation of these broad features is quite consistent with the variety of properties of HACs, which are manifest in a wide range of different spectra depending on their physical and chemical properties (e.g., size, shape, hydrogenation; Scott & Duley 1996; Scott et al. 1997; Grishko et al. 2001). In particular, Grishko et al. 2001 showed that HACs can explain the 21, 26, and 30 μm features. Zhang et al. (2009) also argue that MgS is very unlikely to be the carrier of the aliphatic 30 μm emission seen in C-rich evolved stars. Thus, it is very unlikely that the carriers of the broad 11.5 μm

and 30 μm are related with SiC and MgS, respectively, as was suggested in the past. We tentatively define all these features as aliphatic dust features, found in 22 PNe of our sample.

Three of the CRD spectra in our sample show both aromatic and aliphatic features, thus the total number of CRD PNe in our sample amounts to 38, or ~25% of the PN spectra. All CRD spectra are shown in Figure 4, where we show complete spectra in the left panels of each figure, and the 5–15 μm section of the spectra in the right panels, to characterize the presence (or absence) of AIB features. Most of the CRD
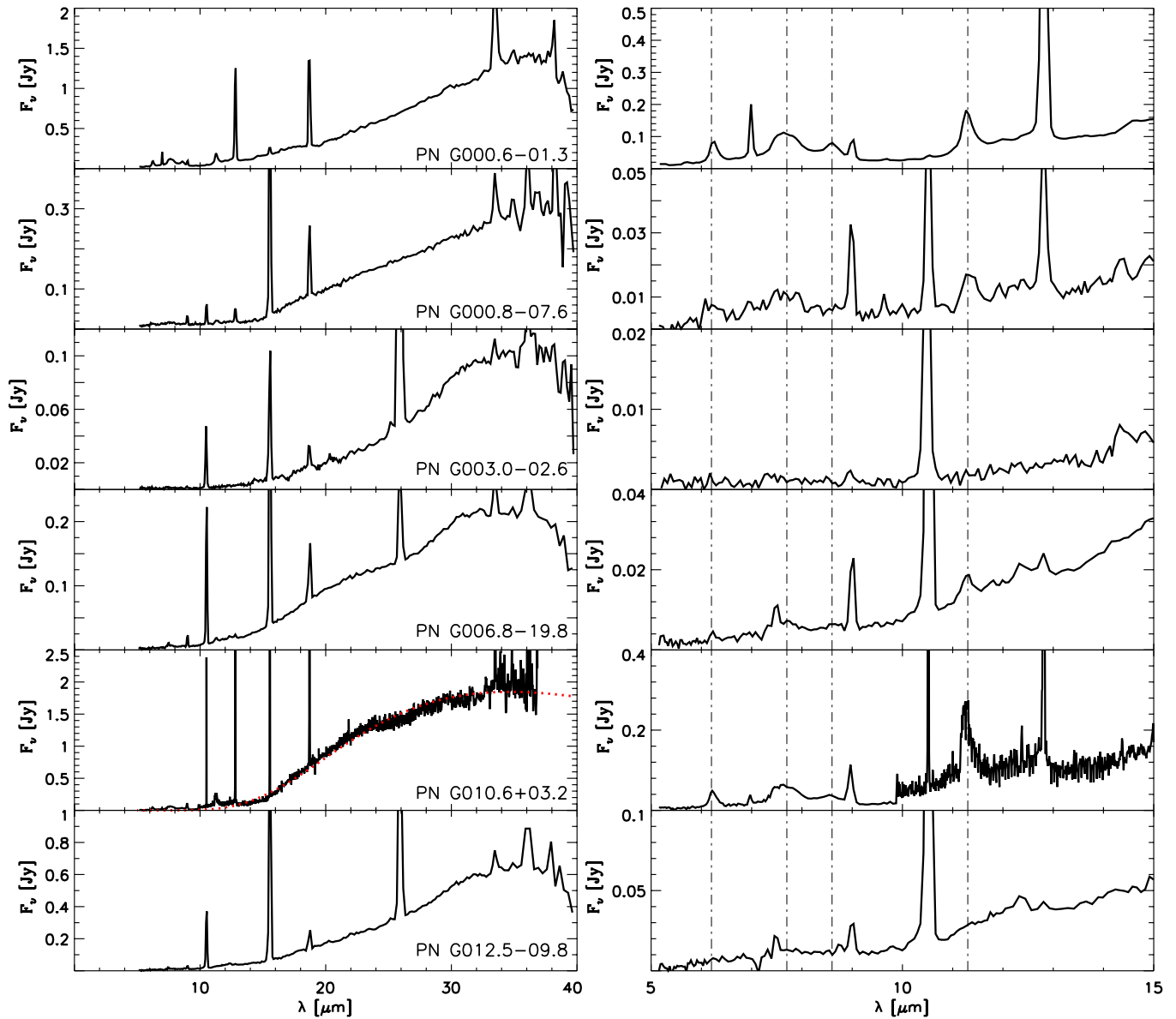
Figure 4. CRD spectra in PN G order. Both aromatic, aliphatic, and aromatic/aliphatic spectra are shown here, see Table 3 for complete list. In the left panels, we show the complete spectra, while right panels show the 5–12 μm sections of the spectra, where the 6.2, 7.7, 8.6, and 11.2 μm AIB band positions have been indicated with vertical lines. Dotted lines have the same meaning as in Figure 3.

(An extended, color version of this figure is available in the online journal.)

spectra are predominantly aromatic or aliphatic, as noted in Column 3 of Table 3. In a few cases, both sets of features are present, and we mark the PN as aromatic/aliphatic type. In a minority of cases, the CRD dust features are very faint, and had the spectra been shallower we would have classified them as F. Their dust type in Column 3 of Table 3 is then flagged as uncertain. Interestingly, two CRD aliphatic PNe, PN G063.8−03.3 and PN G235.3−03.9, display strong C_{60} fullerene features (García-Hernández et al. 2010), and are part of a small group of Galactic and Magellanic Cloud PNe that show the infrared emission bands of this complex molecule (Cami et al. 2010; García-Hernández et al. 2010, 2011a). PNe that contain fullerenes are typically low-excitation and low-mass C-rich objects displaying the broad 11.5 and 30 μm aliphatic features. The detection of fullerenes in the H-rich circumstellar shells of these PNe (see also García-Hernández et al. 2011b) has challenged our understanding of the formation of these complex

fullerene molecules in space, indicating that fullerenes may be more abundant than previously believed and demonstrating that normal C-rich PNe are important factories of complex organic compounds.

Carbon-rich dust features have been found in 42 additional PNe, where crystalline silicate bands (e.g., Waters et al. 1998) are also present. These objects, MCD PNe, showing both AIBs (C-rich) and crystalline silicates (O-rich) in their shells (e.g., Perea-Calderón et al. 2009), have not been found in the Magellanic Clouds to date (S07; Bernard-Salas et al. 2009), but are very common in the Galactic bulge (Gutenkunst et al. 2008; Perea-Calderón et al. 2009). A template spectrum of MCD-type PNe is shown in Figure 2, while all other MCD PN spectra are presented in Figure 5, where we show complete spectra in left panels, and the 5 μm < λ < 15 μm spectra in the right panels, as in the CRD PN spectra. In the MCD PN plots, we also indicate the prominent crystalline silicate
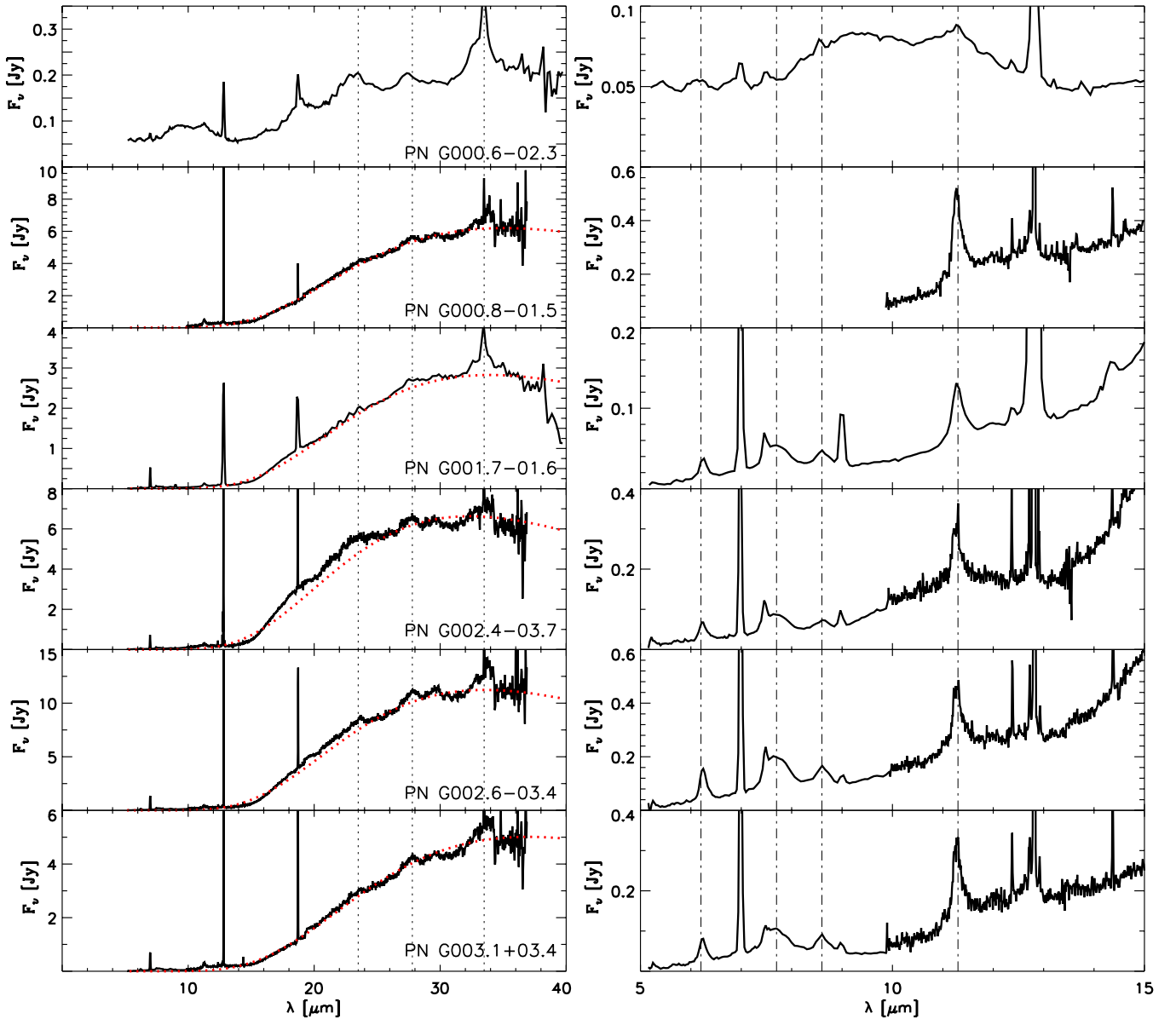
Figure 5. MCD spectra in PN G order. In the left panels, we show the complete spectra, where the crystalline silicate bands at 23.5, 27.5, and 33.8 μm have been marked with vertical dotted lines; right panels show the 5–12 μm sections of the spectra, where the 6.2, 7.7, 8.6, and 11.2 μm AIB band positions have been indicated with vertical lines. Dotted lines have the same meaning as in Figure 3.

(An extended, color version of this figure is available in the online journal.)

features at 23.5, 27.5, and 33.8 μm—usually attributed to olivine and pyroxenes—with vertical dotted lines. Crystalline silicates and other oxygen-rich dust features (e.g., the amorphous silicate bands at ∼10 and 18 μm), not associated with carbon-rich dust, have been detected in 45 PNe. Of these, 16 have only crystalline silicate features, 24 show possible amorphous oxygen features, and five show possible signatures of both types (amorphous and crystalline) of oxygen-rich dust. We call all these objects ORD (oxygen-rich dust) PNe. The details of their subtypes are given in Table 2, and their spectra are shown in Figure 6.

It turns out that 7 of the 157 targets acquired by us are mis-classified as PNe, thus their spectral analysis will be published elsewhere. The IRS spectra of the remaining 150 Galactic PNe indicate that many more show dust features than their Mag-

ellanic Cloud counterparts, as expected, given their relative metallicities (S07). Only ∼17% of the Galactic sample does not show molecular/dust features, while the featureless PNe in the Clouds represented >41% of the samples (S07; Bernard-Salas et al. 2009). The PNe spectra with molecular/dust features in the Galaxy are distributed evenly among the ORD, CRD, and MCD types, respectively, representing approximately 30%, 25%, and 28% of the sample; in the Magellanic Clouds, on the other hand, most of the dust-rich PN spectra are CRD, and only very few PNe show ORD features, while MCD PNe have not been detected in the Magellanic Clouds. A more de-tailed analysis (e.g., integrated fluxes, positions, etc.) of the organic (AIBs) and solid-state features (aliphatic dust, amor-phous, and crystalline silicates) seen in our Galactic Disk PN sample in comparison to those of the Magellanic Clouds will be
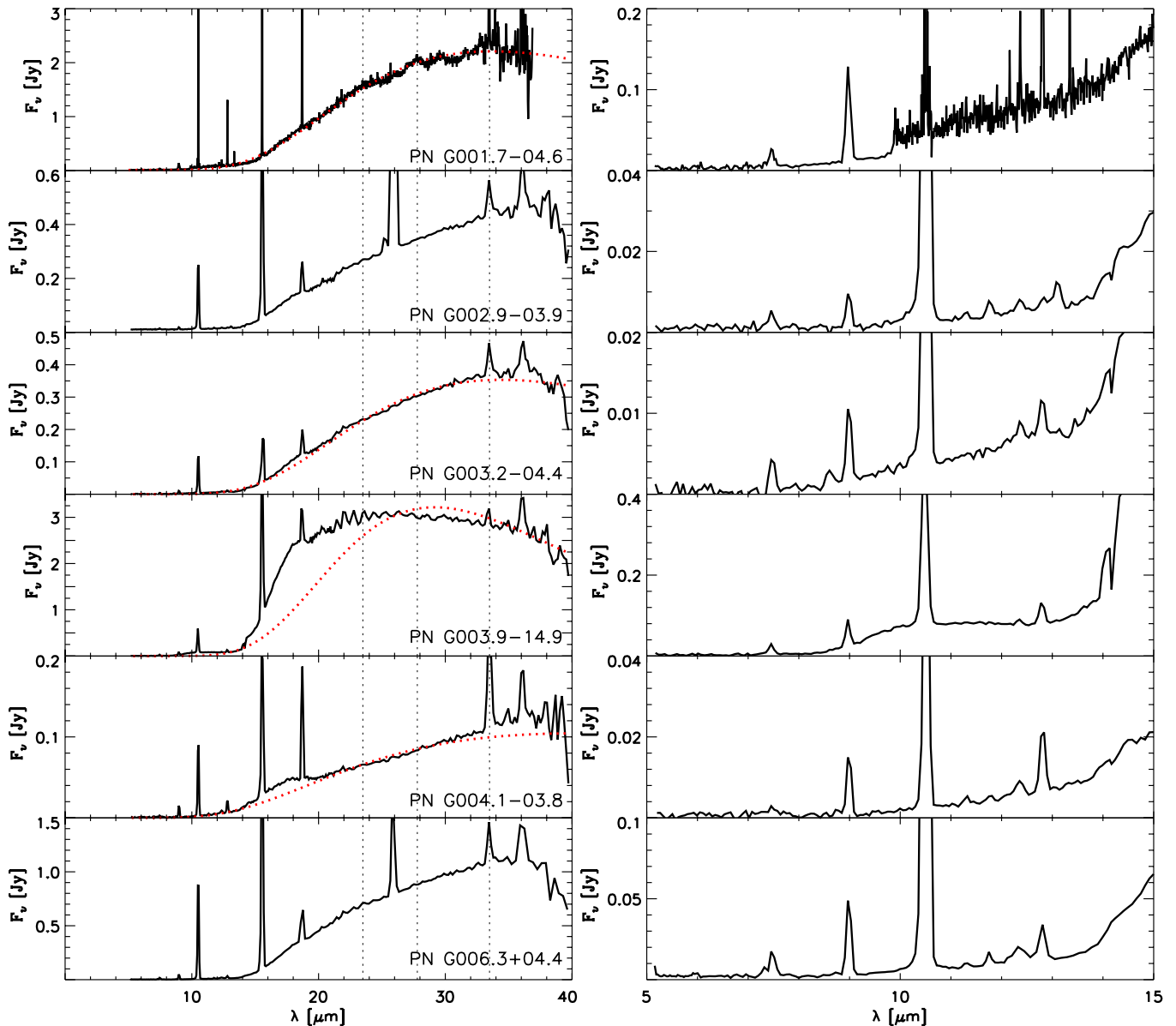
Figure 6. ORD spectra in PN G order. In the left panels, we show the complete spectra, where the crystalline silicate bands at 23.5, 27.5, and 33.8 μm have been marked with vertical dotted lines; right panels show the 5–12 μm sections of the spectra. Dotted lines as in Figure 3.

(An extended, color version of this figure is available in the online journal.)

presented in a forthcoming paper (D. A. García-Hernández et al., in preparation).

4. CORRELATIONS BETWEEN IR SPECTRAL CHARACTERISTICS AND OTHER NEBULAR AND STELLAR PROPERTIES

4.1. Ancillary Data from the Literature

From the IRS analysis in this paper, we have acquired the knowledge of several IR-related properties of the PNe. In Table 3, together with the class and subclass of the dust spectra, we give the IRS-spectra-related parameters, namely, the fit type (Column 4), the emissivity exponent (Column 5), the 60–65 μm flux from the Akari or *IRAS* surveys used to assess the validity of the continuum fit (Column 6), the dust temperature and its uncertainty (Column 7), the total IR luminosity (Column 8), and the infrared excess (IRE), derived classically as in Pottasch (1984) (Column 9). Dust temperatures are given only in the

cases where the blackbody fits converge, either with simple blackbody or with an emissivity term. It is worth noting that the different dust types show a difference in emissivity, as expected, with the average of the exponent α in CRD PNe being 0.52 ± 0.73, compared to an average value of 3.16 ± 2.06 in ORD PNe. The infrared luminosity was determined by integrating the flux under the blackbody fit of the IRS dust continua, then scaled to absolute luminosity by using the statistical distances. The PNe whose fits converge may have an *A, B,* or *C* fit type (Column 4), as described in Section 3. In Figures 9 and beyond, we plot T_{dust} and L_{IR} only in the case of an *A* or *B* blackbody fit type.

Other properties of the PNe that we have used in this study have been listed in Table 4. The most important parameter to gain astrophysical insight from the analysis of PN properties is of course their distances. Individual heliocentric distances determined with reliable methods, such as cluster membership, are not available for most of the PNe in our sample. We then use the best statistical distance scale available, based on the
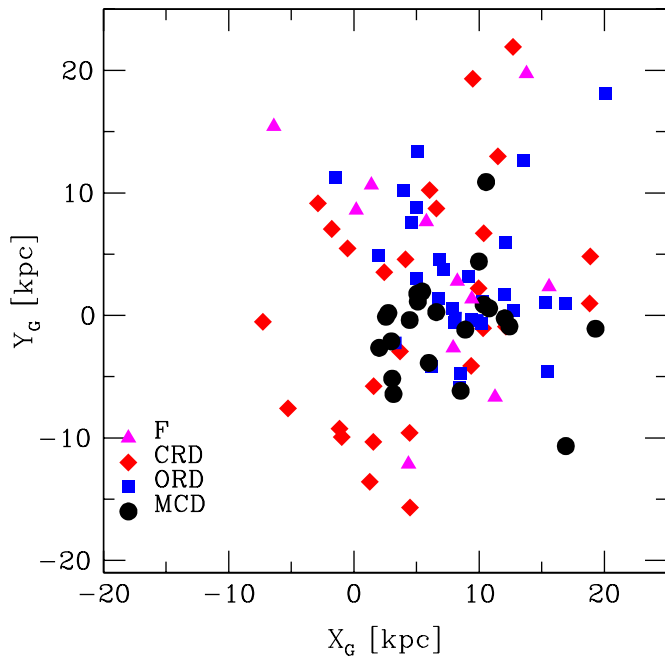
14

Figure 7. Galactic X and Y location for F (triangles), CRD (diamonds), ORD (squares), and MCD (circles) PNe. It appears that most MCD PNe are more centrally concentrated than other types.

(A color version of this figure is available in the online journal.)

Stanghellini et al. (2008) Magellanic Cloud calibration. In order to get statistical distances on this calibrating scale, we need the angular diameters and the 5 GHz (or Hβ) fluxes. The fluxes, and the upper limits to angular diameters, are available for all targets, but actual angular diameters are known only for 50 of the 150 confirmed PNe in our IRS sample, thus their distances are readily available only for approximately a third of the sample (see also Stanghellini & Haywood 2010). An additional 42 PNe have been observed by us with WFC3 (R. A. Shaw et al., in preparation), and from these space-based images we were able to derive the angular sizes, and thus calculate their distances with the statistical scheme described above. Distances from the Galactic center, and the PN sizes derived as described in Stanghellini & Haywood (2010), are listed in Table 4.

Plasma diagnostics for the observed PN based on optical spectra are scarce in the literature, with only a dozen PNe having adequate electron density and elemental abundance. We have used the [S II] $\lambda6717$–6731 emission lines measured from low-resolution spectroscopy and published by Acker et al. (1992) to derive an estimate of the nebular densities, by assuming electron temperatures of 10,000 K and by using the *nebular* routines in *IRAF/stsdas* (Shaw & Dufour 1995). The densities calculated are listed in Column 4 of Table 4. There is not enough information to determine oxygen or other abundances for most of the compact PNe in our sample. The abundance analysis based on the IR lines in the IRS spectra will be the subject of a future paper.

For all other nebular parameters, we used the Stanghellini & Haywood (2010) recent, complete, and uniform collection of Galactic PN data.

4.2. Segregation and Evolution of Dust Types

In Figure 7, we show the distribution of dust types as projected on the Galactic plane, where $X_G = D \cos(b) \cos(l)$, $Y_G = D \cos(b) \sin(l)$, D is the heliocentric distance, and l and b are,

respectively, the Galactic longitude and latitude. Diamonds represent the CRD, squares the ORD, triangles the F, and circles the MCD PNe. It appears that there is mild segregation of dust type within the Galactic distribution, in particular the MCD PNe tend to be concentrated within the plot. To explore this segregation further in Figure 8, we show the histograms of dust types as they are distributed in relation of their distance from the Galactic center, and we recover the accumulation of MCD PNe with $R_G < 9$ kpc, unlike the other dust types. CRD and ORD PNe seem to be rather uniformly distributed.

Of the three (possible) halo PNe in our sample, two belong to the CRD class, both with aliphatic features, while one shows ORD features. We do not observe a spatial segregation of the CRD dust subtypes. On the other hand, by examining the latitude distribution of the ORD subtypes, we find that the crystalline ORD PNe have typically lower Galactic latitude ($\langle|b|\rangle = 2.95 \pm 1.76$) than the amorphous ORD PNe ($\langle|b|\rangle = 6.33 \pm 3.51$). This is consistent with the former type of ORD PNe being the progeny of high-mass AGB stars, while the latter are possibly the remnants of the lowest mass progenitors.

It is worth noting that PN samples in the Galactic bulge, such as those studied by Gutenkunst et al. (2008) and Perea-Calderón et al. (2009), show a majority of dual-chemistry PNe, unlike other known samples. Our Galactic disk sample broadly selects against bulge PNe, but the mere definition of Galactic bulge PN (e.g., Stanghellini & Haywood 2010) is affected by the PN apparent angular radii, which can be very uncertain for compact PNe. By using the definition of bulge PN by Stanghellini & Haywood (2010), we determine that 26 of our 150 PNe might belong to the bulge. We will discuss in more detail the dust properties of bulge, disk, and Magellanic Cloud PNe. In the following analysis, and in all subsequent plots, we exclude potential bulge PNe from the Galactic sample.

In Figure 9, we show the dust temperature plotted against the linear size of the PNe in our sample whose dust temperature and distances are available. Different type PNe are plotted with different symbols (see Figure 7 legend), and temperature error bars are also plotted, while a typical error bar for the radii is given in the plot. At zeroth order, if all PN progenitors were of identical mass and metallicity, and if the PNe expand at a constant expansion velocity, then one would expect $\log T_{\rm dust} \propto -0.4 \log R_{\rm PN}$ if the dust grains do not evolve in size (see, e.g., Lenzuni et al. 1989). In the snapshot of evolutionary stages provided by a sizable observational sample, we see the scatter due to the different dust types, masses, metallicity, shell acceleration, and alternative evolutionary paths. It appears that the CRD PNe are concentrated toward the high dust temperatures across a wide domain of radii. Furthermore, there is a rather tight correlation between dust temperatures and physical radii of CRD PNe, with a correlation coefficient of -0.99, which is suggestive of a rather narrow initial mass and metallicity range. The slope of the CRD PNe on this plane is shallower than that found for non-evolving grains (Lenzuni et al. 1989), suggesting that there is some type of evolution of the dust grains in CRD PNe.

The solid line in Figure 9 represents the least-squares fit for the CRD PNe, $\log T_{\rm dust} = -0.250 \log R_{\rm PN} + 6.41$, where the temperatures are measured in K and the nebular sizes in cm. The ORD PNe do not follow a narrow sequence in this plane. A possible explanation for the markedly different domains of dust temperatures in CRD and the bulk of ORD and MCD PNe could reside in the different heat capacity of dust grains as function of
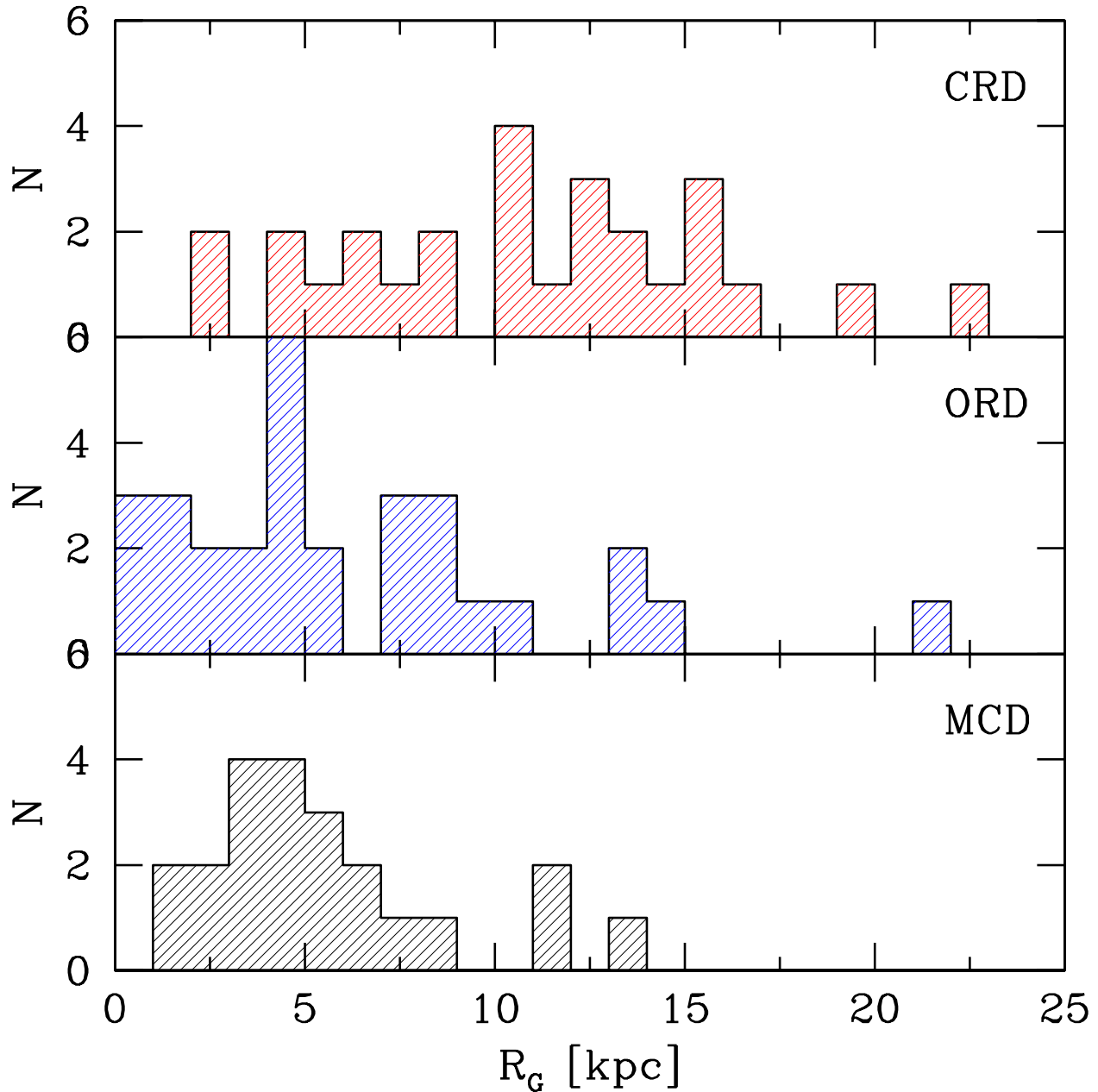
Figure 8. Distribution of the distances to the galactic center for CRD (top), ORD (middle), and MCD (bottom) dust PNe.
(A color version of this figure is available in the online journal.)

grain size and composition. Li & Draine (2001) have shown that equilibrium temperatures of small carbonaceous grains are generally higher than for silicate grains in the interstellar medium (ISM). PN dust should behave similarly to the ISM one, as the ISM is mostly composed by recycled dust from the evolution of LIMS, thus this could explain the observed distribution of temperatures of the CRD versus the other dust-type PNe.

In Figure 10, we show the dust temperature versus the IR luminosity (in solar units) as determined from the blackbody fits of the continua. In this plot, the CRD PNe are found in a sequence, where PNe characterized by hot dust are more luminous in the IR. On the other hand, ORD and MCD PNe are found scattered on this plane. If, for example, we look at PNe with $\log L_{IR}/L_\odot > 3$, we find several very hot CRD PNe, while both ORD and MCD PNe have low/intermediate dust

temperatures. This effect could be dominated by the different heat capacity of the carbon-rich and oxygen-rich dust grains. There could also be an effect of ORD PNe originating from a range of progenitors, including very massive ones. One would expect to find PNe with low- to intermediate-mass progenitors in the upper right portion of the plot, where we typically find CRD PNe.

In Figure 11, we plot the dust temperature against the nebular electron density. There is no particular segregation among the CRD and ORD or MCD PNe, apart from the high dust temperatures of CRD PNe as noted above.

In Figure 12, we show the IR luminosity of the PNe versus the nebular radius. If we could assume that the expansion velocity is uniform for all PNe, then this plot would represent the evolution of IR luminosity in PNe. The expected decline of luminosity with radius is found as expected from a large PN population.

Table 4
Other PN Parameters

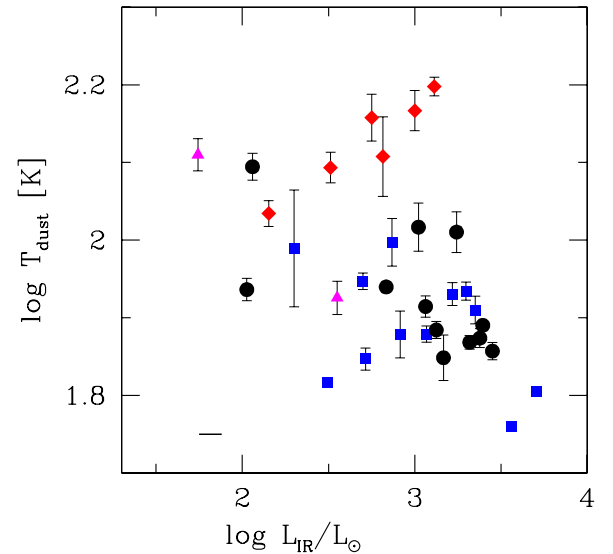| Name	R_G (kpc)	$\log R_{PN}$ (cm)	$\log N_e$ (cm^{-3})	I_{4686} ($I\beta = 100$)	Ne Ratio	EC
(1)	(2)	(3)	(4)	(5)	(6)	(7)
PN G000.3−02.8	...	...	2.511	...	1.257	4.181
PN G000.6−01.3	...	...	3.357	...	−1.204	...
PN G000.6−02.3	...	...	3.280	...	...	...
PN G000.8−01.5	...	...	4.166	...	...	...
PN G000.8−07.6	...	...	3.304	...	1.162	4.415
PN G001.7−01.6	...	...	3.767	...	...	...
PN G001.7−04.6	4.731	17.46	3.787	2.5	1.133	2.839
PN G002.4−03.7	1.439	17.39	4.352	...	...	...
PN G002.6−03.4	...	...	3.722	...	...	...
PN G002.9−03.9	...	...	...	35.0	...	6.260
PN G003.0−02.6	10.880	17.63	...	34.0	...	6.205
PN G003.1+03.4	2.868	17.47	3.215	...	...	...
PN G003.2−04.4	8.955	17.55	...	...	1.516	4.127
PN G003.9−14.9	0.547	17.39	3.722	...	1.801	3.740
PN G004.1−03.8	7.424	17.57	...	...	1.097	4.095
PN G004.3−02.6	5.251	17.71	...	...	0.460	2.209
PN G004.9−04.9	2.521	17.50	3.428	...	−0.548	0.112
PN G005.5+0.27	...	...	...	...	...	0.814
PN G006.0+02.8	...	...	2.707	...	...	...
PN G006.3+04.4	2.515	17.47	...	4.5	1.829	6.422
PN G006.8+02.0	...	...	...	...	0.292	1.696
PN G006.8−19.8	...	...	3.206	13.4	...	5.064
PN G007.5+04.3	...	...	...	...	...	1.255
PN G008.1−04.7	4.401	17.47	3.240	...	0.733	2.416
PN G008.2−04.8	1.967	17.46	3.240	...	1.516	4.181
PN G008.6−02.6	...	...	...	...	1.614	4.477
PN G008.6−07.0	7.938	17.55	2.825	15.0	1.264	5.152
PN G009.3+04.1	...	...	...	...	1.535	4.851
PN G010.6+03.2	...	...	4.114	...	0.316	1.561
PN G011.1+07.0	...	...	...	50.0	...	7.091
PN G011.3−09.4	1.822	16.98	4.114	...	−1.220	0.283
PN G011.7−06.6	4.816	17.79	4.270	...	...	...
PN G012.5−09.8	2.959	17.45	...	7.8	...	5.845
PN G012.6−02.7	3.112	17.59	4.058	...	...	...
PN G014.0−05.5	...	...	...	29.0	1.671	5.928
PN G014.3−05.5	11.900	17.12	3.722	5.9	...	1.975
PN G016.9−02.0	...	...	3.508	...	1.477	7.537
PN G018.6−02.2	2.796	17.56	...	47.0	1.802	6.925
PN G019.2−02.2	3.370	16.94	3.852	4.0	1.778	8.010
PN G019.4−05.3	3.433	16.86	4.114	...	0.865	4.113
PN G019.7+03.2	3.208	16.78	...	...	1.414	7.956
PN G019.8+05.6	...	...	3.576	28.0	1.449	5.872
PN G023.8−01.7	4.833	17.39	...	...	...	...
PN G023.9+01.2	...	...	3.795	...	...	...
PN G025.3−04.6	...	...	...	...	1.630	5.944
PN G026.0−01.8	7.225	17.42	...	...	1.912	6.934
PN G027.6−09.6	3.825	17.13	...	0.6	1.709	1.660
PN G031.0+04.1	4.238	16.55	...	...	1.575	0.337
PN G032.5−03.2	...	...	...	...	...	0.175
PN G032.9−02.8	7.109	17.05	3.619	...	1.455	8.572
PN G034.0+02.2	4.755	17.37	3.077	...	1.328	6.880
PN G038.4−03.3	...	...	3.162	...	...	...
PN G038.7−03.3	...	...	3.722	11.4	1.894	1.993
PN G041.8+04.4	...	...	...	...	...	0.135
PN G042.0+05.4	21.790	17.31	4.046	...	...	...
PN G042.9−06.9	13.790	17.05	3.428	0.3	1.531	5.184
PN G044.1+05.8	...	...	...	...	...	1.953
PN G045.9−01.9	11.190	17.13	...	...	−0.391	0.977
PN G048.1+01.1	6.010	16.66	3.593	...	1.309	9.328
PN G048.5+04.2	13.460	17.51	...	66.0	...	7.978
PN G051.0+02.8	...	...	...	...	...	6.412
PN G052.9+02.7	8.846	17.72	...	...	1.535	6.759
PN G052.9−02.7	7.962	17.06	...	...	...	8.532
PN G055.1−01.8	20.580	17.70	...	...	1.879	7.371

Table 4
(Continued)

Name	R_G (kpc)	$\log R_{PN}$ (cm)	$\log N_e$ (cm^{-3})	I_{4686} ($I\beta = 100$)	Ne Ratio	EC
(1)	(2)	(3)	(4)	(5)	(6)	(7)
PN G055.5−00.5	6.597	17.09	4.114	. . .	1.252	2.061
PN G058.9+01.3	8.342	17.43	. . .	. . .	1.167	2.389
PN G059.4+02.3	10.420	17.37	. . .	. . .	2.527	6.327
PN G059.9+02.0	22.410	17.11	. . .	. . .	. . .	. . .
PN G060.5+01.8	9.297	17.22	. . .	. . .	−0.055	1.660
PN G063.8−03.3	19.380	17.01	. . .	. . .	. . .	. . .
PN G067.9−00.2	7.743	16.50	3.787	. . .	0.804	1.526
PN G068.7+01.9	10.950	17.41	. . .	. . .	1.898	5.166
PN G068.7+14.8	. . .	. . .	. . .	2.4	. . .	2.682
PN G069.2+02.8	13.670	16.33	. . .	. . .	. . .	0.153
PN G077.7+03.1	. . .	. . .	3.473	. . .	1.044	12.150
PN G079.9+06.4	. . .	. . .	. . .	77.0	. . .	8.587
PN G082.5+11.3	12.530	16.82	. . .	. . .	0.895	1.102
PN G088.7+04.6	11.620	17.45	. . .	. . .	1.846	2.290
PN G095.2+00.7	10.110	17.03	. . .	. . .	1.158	5.648
PN G097.6−02.4	14.730	17.57	. . .	7.0	2.041	5.935
PN G104.1+01.0	12.060	16.88	. . .	. . .	0.913	6.476
PN G107.4−00.6	. . .	. . .	. . .	. . .	. . .	0.410
PN G107.4−02.6	14.200	17.62	. . .	92.0	. . .	9.418
PN G112.5−00.1	21.100	17.68	2.033	. . .	0.833	1.418
PN G184.0−02.1	15.270	17.09	. . .	. . .	0.012	. . .
PN G205.8−26.7	. . .	. . .	. . .	. . .	. . .	4.045
PN G235.3−03.9	15.260	17.10	4.689	. . .	. . .	0.072
PN G263.0−05.5	12.990	17.31	3.762	9.2	1.915	5.598
PN G264.4−12.7	13.390	17.33	3.949	. . .	0.750	2.723
PN G274.1+02.5	. . .	. . .	. . .	. . .	. . .	1.620
PN G275.3−04.7	15.170	17.33	. . .	28.0	. . .	5.872
PN G278.6−06.7	12.160	17.23	3.619	6.0	1.887	6.354
PN G285.4+01.5	8.625	17.27	4.114	. . .	0.601	5.656
PN G285.4+02.2	. . .	. . .	2.909	78.0	. . .	8.642
PN G286.0−06.5	16.060	17.01	3.348	. . .	1.391	4.419
PN G289.8+07.7	12.660	17.39	. . .	45.0	. . .	6.814
PN G294.9−04.3	10.210	17.11	. . .	. . .	−0.994	0.661
PN G295.3−09.3	. . .	. . .	. . .	. . .	1.362	4.338
PN G296.3−03.0	8.029	17.12	3.852	19.0	1.475	5.374
PN G297.4+03.7	. . .	. . .	3.299	. . .	−1.256	0.162
PN G300.7−02.0	7.140	17.21	4.368	. . .	1.002	4.815
PN G307.5−04.9	6.532	17.50	3.787	0.5	0.034	1.323
PN G309.0+00.8	. . .	. . .	. . .	. . .	0.773	4.995
PN G309.5−02.9	. . .	. . .	3.302	. . .	1.563	6.934
PN G311.1+03.4	. . .	. . .	. . .	. . .	0.289	0.608
PN G321.3+02.8	5.232	17.03	4.647	. . .	0.226	3.213
PN G324.2+02.5	6.178	17.37	4.053	. . .	. . .	. . .
PN G324.8−01.1	5.434	16.98	. . .	. . .	1.352	5.769
PN G325.0+03.2	5.935	17.09	3.366	. . .	1.543	6.530
PN G325.8−12.8	5.207	17.49	. . .	. . .	−0.057	0.486
PN G326.0−06.5	4.562	17.45	. . .	. . .	. . .	. . .
PN G327.1−01.8	4.366	17.29	4.114	. . .	−1.617	0.198
PN G327.8−06.1	13.910	17.48	3.677	. . .	0.553	2.362
PN G327.9−04.3	. . .	. . .	3.308	. . .	. . .	5.062
PN G329.4−02.7	7.433	17.47	2.782	. . .	1.702	4.270
PN G331.0−02.7	4.750	17.34	4.339	. . .	−0.703	0.666
PN G334.8−07.4	. . .	. . .	. . .	. . .	−0.794	0.688
PN G336.3−05.6	4.326	17.36	3.722	56.0	1.120	7.424
PN G336.9+08.3	. . .	. . .	. . .	. . .	. . .	4.415
PN G340.9−04.6	. . .	. . .	. . .	. . .	1.902	6.322
PN G341.5−09.1	2.659	17.50	3.206	. . .	1.889	4.689
PN G343.4+11.9	8.748	17.51	. . .	19.5	. . .	5.401
PN G344.2+04.7	. . .	. . .	3.619	. . .	−0.020	1.809
PN G344.4+02.8	. . .	. . .	. . .	. . .	. . .	7.628
PN G344.8+03.4	. . .	. . .	3.306	. . .	−0.695	0.437
PN G345.0+04.3	. . .	. . .	. . .	. . .	. . .	. . .
PN G348.4−04.1	. . .	. . .	3.522	. . .	1.427	6.867
PN G348.8−09.0	. . .	. . .	. . .	. . .	0.753	. . .

Table 4
(Continued)

Name	R_G (kpc)	log R_{PN} (cm)	log N_e (cm^{-3})	I_{4686} ($I\beta = 100$)	Ne Ratio	EC
(1)	(2)	(3)	(4)	(5)	(6)	(7)
PN G350.8−02.4	. . .	. . .	4.250	. . .	0.380	1.737
PN G351.3+07.6	. . .	. . .	. . .	. . .	1.004	2.871
PN G351.9−01.9	. . .	. . .	3.449	. . .	1.220	5.665
PN G352.6+03.0	1.464	17.36	3.779	. . .	1.098	4.838
PN G354.2+04.3	2.556	17.49	3.533	. . .	0.142	0.661
PN G354.9+03.5	. . .	. . .	3.141	. . .	−0.027	1.120
PN G355.2−02.5	3.563	17.53	3.895	. . .	0.963	5.252
PN G355.7−03.0	4.252	17.41	3.531	. . .	1.351	4.671
PN G355.9+02.7	4.518	17.27	4.101	. . .	1.257	6.313
PN G356.2−04.4	0.540	17.31	. . .	4.5	1.677	2.439
PN G356.5+01.5	2.253	17.56	. . .	. . .	0.433	1.854
PN G356.5−03.6	. . .	. . .	3.408	. . .	1.173	3.672
PN G356.8+03.3	11.350	17.42	. . .	. . .	−1.377	0.211
PN G357.1+01.9	. . .	. . .	2.413	. . .	1.324	2.259
PN G357.1−06.1	. . .	. . .	2.879	74.0	0.998	8.421
PN G357.2+02.0	. . .	. . .	3.762	. . .	1.536	9.364
PN G357.6+01.7	1.896	17.32	4.060	. . .	1.390	5.787
PN G357.6+02.6	5.437	17.68	. . .	. . .	1.359	5.126
PN G358.2+03.6	1.449	17.35	3.583	14.5	1.675	5.124
PN G358.3+01.2	. . .	. . .	3.839	. . .	1.058	11.772
PN G358.5+02.9	. . .	. . .	. . .	. . .	. . .	8.496
PN G358.5−04.2	0.237	16.86	4.114	. . .	0.167	2.430
PN G358.6+01.8	. . .	. . .	. . .	. . .	1.605	12.150
PN G358.7+05.2	. . .	. . .	. . .	. . .	. . .	6.066
PN G358.7−02.7	3.723	17.36	3.792	. . .	. . .	. . .
PN G358.9+03.4	4.051	17.10	3.073	. . .	0.089	2.020
PN G358.9−03.7	. . .	. . .	3.058	. . .	−0.375	0.445
PN G359.3+03.6	. . .	. . .	. . .	. . .	1.337	7.758
PN G359.4+02.3	. . .	. . .	4.114	. . .	. . .	. . .

(This table is also available in a machine-readable form in the online journal.)
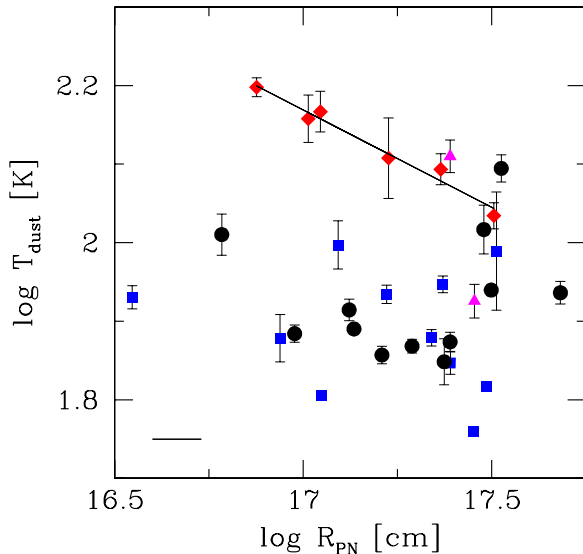
Figure 9. Dust temperature plotted against linear nebular radii (in cm); Galactic disk sample. Symbols are as in Figure 7. The solid line corresponds to the best fit to the CRD PNe. The error bars for T_{dust} have been derived from the continuum fits. The error bar on the left corner indicates a reasonable guess derived from the statistical distance uncertainty, corresponding to $\Delta d = 0.26$.

(A color version of this figure is available in the online journal.)

Figure 10. Dust temperature vs. the integrated IR luminosity. Symbols are as in Figure 7. The error bars have the same meanings as in Figure 9.

(A color version of this figure is available in the online journal.)

Qualitatively, if the luminosity of the CS is mostly radiated through the dust continuum, and if the expansion is uniform

and non-accelerated, then we can compare this plot with the log $L/L_\odot$ versus t [yr] plot in Stanghellini & Renzini (2000, Figure 2 therein) and we see a correspondence.

It is well known that nebulae and CS should be studied together to gain insight on their evolution and progenitor types.
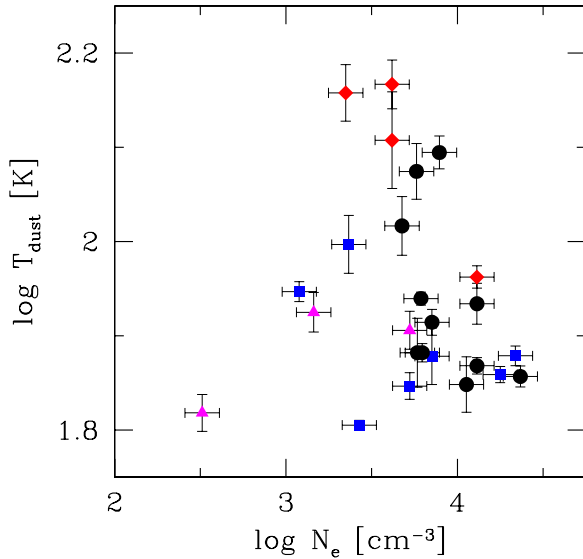
Figure 11. $T_{\rm dust}$ vs. electron density, calculated from [S II] lines. Symbols are as in Figure 7. Temperature error bars are as in Figure 9, and for the electron densities it is assumed a 0.1 dex error (see the text).

(A color version of this figure is available in the online journal.)

Figure 12. IR luminosity against nebular radius, in pc. Symbols are as in Figure 7. The error bar on the left lower corner includes the assumption of a typical distance uncertainty from the statistical distance derivation.

(A color version of this figure is available in the online journal.)

Figure 13. PN excitation class, from optical emission lines (see the text), vs. the ratio of the IR line intensities of [Ne III] at $\lambda 15.56\,\mu$m and [Ne II] at $\lambda 12.81\,\mu$m. Symbols are as in Figure 7.

(A color version of this figure is available in the online journal.)

In the Galactic sample presented here, the information about the CS is still very scarce. Given the compactness of the PNe in our sample, their CS magnitudes are typically unreachable from the ground, and the standard methods of temperature determinations from the Zanstra analysis are thus not applicable. Spectral types, on the other hand, are available for only very few CS of each dust class, thus correlations are not statistically sound. By correlating the CS spectral types (Weidmann & Gamen 2011) with the dust classes in this paper, we noted that CS of the CRD PNe are of the *wels* type in 6 of the 10 available spectra for this dust class, while most of the ORD PNe have Of or O(H) CS (8 of the 12 available spectra). While there is certainly a mild correlation between CS and dust class, the samples are too small to draw robust evolutionary scenarios.

For a sizable part of the sample, there will be high quality *HST* magnitudes available in the near future from the WFC3 images collected by us (R. A. Shaw et al., in preparation). For high-excitation PNe, those whose CS are hot enough to doubly ionize nebular helium, we can use the He II $\lambda 4686$ flux as a probe of stellar temperature. In Table 4, Column 5, we list the $\lambda 4686$ intensities found in the literature (see selection in Stanghellini & Haywood 2010), but the sample that includes reliable fluxes and dust parameters (temperature, IR luminosity) is too small for meaningful comparative analysis.

We can use other criteria to characterize the hardness of the UV radiation of the CS with both IR and optical nebular emission lines. For example, Morgan (1984) showed that a good measure of the hardness of the ionizing stellar flux in a PN was the excitation class, or EC, derived as EC $= 0.45\ I_{\lambda 5007}/I_\beta$ for those PNe whose CS are not sufficiently hot to produce He II nebular emission, and EC $= 5.54\ (I_{\lambda 4686}/I_\beta +0.78)$ for the high-excitation PNe. An estimate of the hardness of the UV field could also be obtained directly from the IRS spectra, for example, by using the [Ne III] (15.56 μm) to [Ne II] (12.81 μm) line flux ratio (Bernard-Salas et al. 2009). We list both the neon ratio described above, calculated using our analysis of the IRS emission line spectra (L. Stanghellini et al., in preparation), and the excitation constant, calculated using the parameters in Stanghellini & Haywood (2010), in Table 4. Naturally, neither
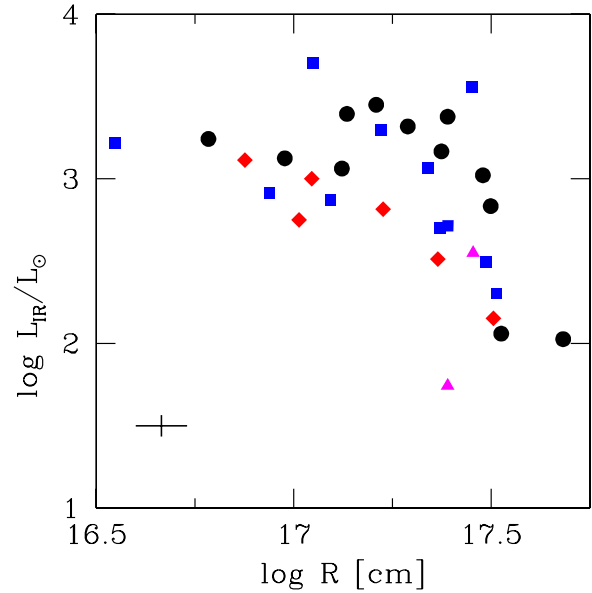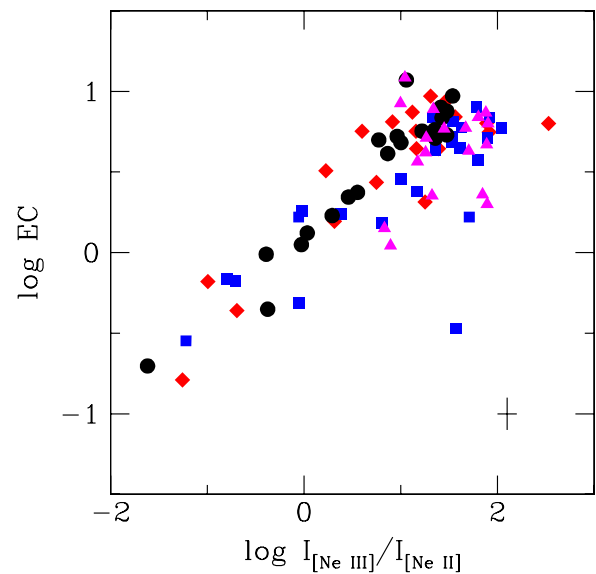
of these criteria are ideal substitutes for a direct measurement of the stellar temperature, or even for an indirect measurement such as the stellar temperatures derived via the Zanstra method. For example, the neon flux ratio from IR emission lines is a reasonable stellar flux tracer only for intermediate-excitation nebulae. Furthermore, the neon intensity ratio method fails if the PN is lumpy, non-homogeneous, or weather shocks dominate the emission.

The [Ne III]/[Ne II] line ratio from the IRS spectra is a rough indication of the PN evolutionary stage, if the effects of shocks are absent or moderate. In fact, depending on where the line originates within the nebulae, this ratio is tightly correlated with the excitation class or not, and the difference is expected to be larger in PNe with complicated shapes. In Figure 13, we show

Table 5
Morphological Distribution Among Dust Types

Dust Type	N	R %	E %	Symm. %	BC %	B %	P %	Asymm. %
(1)	(2)	(3)	(4)	(5)	(6)	(7)	(8)	(9)
F	5	...	80	80	20	...	...	20
CRD	24	13	61	74	4.2	17	4.2	26
ORD	17	12	35.3	47	...	35.3	18	53
MCD	12	...	50	50	...	25	25	50

Table 6
Galactic Bulge, Disk, and Magellanic Cloud PN Dust Class Distribution

Dust Type (1)	Bulge, % (2)	Galactic, % (3)	Magellanic Clouds, % (4)
F	4	20	41
CRD	11	28	52
ORD	38	28	7
MCD	46	24	N.A.

how the excitation class derived from the optical emission lines correlates quite well with the UV flux-sensitive neon intensity ratio. We observe in the figure that the neon ratio is a better estimate of the PN excitation class in CRD and MCD PNe, where it correlates with the excitation constant with correlation coefficients (between the two logarithmic values) of 0.88 and 0.94 for the CRD and the MCD PNe, respectively. On the other hand, the correlations are more scattered for ORD PNe, where the overall correlation coefficient between the two logarithmic values is 0.75, and at high excitation the correlation is very scattered. This finding complies with the hypothesis that in high-excitation ORD PNe, the neon ratio is not a good indicator of the hardness of the stellar flux. The explanation could lie in the asymmetric morphological type of a good fraction of ORD PNe, which was hinted at in the Magellanic Cloud sample.

The morphologies of our sample of Galactic PNe according to their dust type are illustrated in Table 5, where we list, for each dust class, the number of PNe in each of the major morphological classes, following the classification scheme by Stanghellini et al. (2002). Sequentially, we give in the table the percentage of PNe in the separate categories of round (R), elliptical (E), bipolar core (BC), bipolar (B), and point-symmetric (P) PNe, as well as the cumulative classes of *symmetric* (round/elliptical) and *asymmetric* (bipolar/bipolar core/point-symmetric) PNe. It is clear that the few F PNe in this table do not constitute a statistically significant sample. Among the other dust types there are some notable differences in the morphological distribution: CRD PNe are for the major part morphologically symmetric, with just a quarter of the sample displaying asymmetric features; on the other hand, both ORD and MCD PNe are almost equally distributed among the symmetric and asymmetric classes. It is also worth noting that the peculiar class of point-symmetric PNe are well populated by MCD targets, a very interesting coincidence of two peculiarities which is worth further study.

5. COMPARISON OF THE GALACTIC AND THE MAGELLANIC CLOUD PN SAMPLES

In the previous sections, we have shown the atlas of the spectra of ∼150 compact Galactic PNe that we plan to study in much more detail. In this data paper, we aim to show the general characteristics of this sample, and compare it to the Magellanic Cloud PN IRS sample. Group and subgroup properties have been illustrated above; here, we discuss what could be the leading evolutionary paths and the progenitor characteristics that might lead to the observed configuration. A thorough analysis of these issues is planned for a future paper.

The first notable comparison between the Galactic and Magellanic Cloud samples is the statistical distribution of dust types within the different environments. In Table 6, we give for each main dust class, the PN frequency in the Galaxy (this paper, consisting in 150 PNe, 26 of which might be bulge PNe) and

in the Magellanic Clouds, where both the S07 and the Bernard-Salas et al. (2009) samples have been included, for a total of 66 PNe in both Clouds. The major selection difference from the targets in the samples is the compactness of Galactic PNe, while the Magellanic Cloud PNe have been selected on PN optical brightness. Given the tight correlation between physical size and brightness, we assume that the selection criteria will not affect the following discussion. Of the 150 Galactic PNe, only 25 do not show notable molecular/dust features in their spectra, apart from a weak dust continuum, while in the Magellanic Cloud F PNe are ∼41% of the sample. Sloan et al. (2008) showed that the number of evolved, dust-free stars increases with decreasing metallicity, broadly in agreement with our findings.

Among the spectra with notable grain features, Galactic PNe are distributed almost uniformly among the CRD, ORD, and MCD dust classes. In the Magellanic Clouds, on the other hand, most PNe are CRD, only a few are ORD, and none have MCD. In S07, we showed that the CRD PNe are also enriched in gas-phase carbon, and they represent the progeny of the intermediate mass in the PN progenitor range. The results of Table 6 indicate that PNe evolving from Magellanic Cloud progenitors are more likely to have carbon-rich dust than Galactic PNe, probably indicating that the Galactic disk PN progenitors are on average more massive than their homologous in the Clouds. Interestingly, none of the IRS observations of Magellanic Cloud PNe (including those by different authors) show any indication of MCD class PNe, while this type is notable in the Galaxy. Whatever the mechanism to produce MCD PNe, it does not appear to be efficient at the Magellanic Cloud metallicity.

The PNe in our Galactic sample that might belong to the bulge have characteristics that are even more extremely different from the Magellanic Clouds than those of Galactic disk PNe. In fact, nearly all bulge PNe have dust features, and only 11% of them have CRD types, while ORD (38%), and especially MCD (46%) PNe are the majority. There seems to be continuity of dust class distribution from the bulge, to Galactic disk, to Magellanic Cloud PNe, where all the class frequencies change monotonically from one population to the next. It seems that metallicity plays a fundamental role in this picture: going from high (the bulge is α-element enriched with respect to the Galactic disk, Zoccali et al. 2006) to low (the Magellanic Clouds are half or quarter solar in α-element abundances) metallicity, the number of dust-rich PNe decreases, as does the fraction of PNe with ORD and MCD, while the number of CRD PNe increases.

In Figure 14, we show the dust temperature versus physical radii of the Galactic disk (filled symbols) and the Magellanic Cloud (open symbols) PNe, respectively, from this paper (Galactic disk only) and S07. Given that we did not find MCD PNe in the Magellanic Clouds and that the ORD PNe were a striking minority, here we only plot the F and CRD PNe for a meaningful comparison of the two samples. Distances, and consequently linear radii, are very sound for Magellanic Cloud
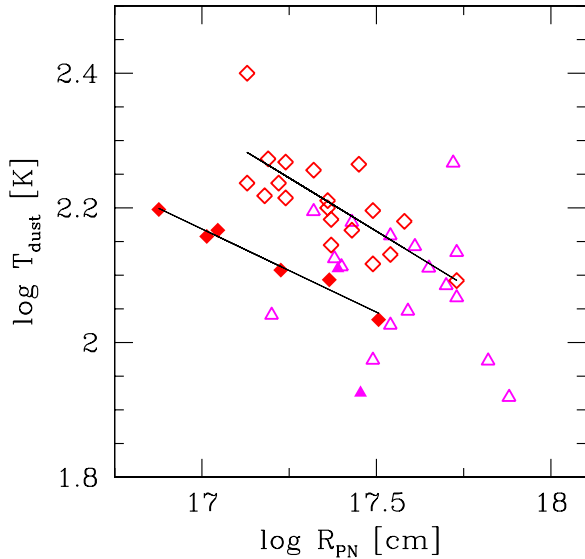
Figure 14. Dust temperature plotted against linear nebular dimensions (in cm). Triangles: F, diamonds: CRD. Filled symbols represent Galactic PNe. Open symbols represent the Magellanic Cloud sample from S07. Solid lines: best fit to the CRD PN loci in the two samples.

(A color version of this figure is available in the online journal.)

Figure 15. Dust temperature vs. the integrated IR luminosity for Galactic and Magellanic PNe. Symbols are as in Figure 14.

(A color version of this figure is available in the online journal.)

Figure 16. T_{dust} vs. electron density, calculated from [S II] lines, for Galactic and Magellanic PNe. Symbols are as in Figure 14.

(A color version of this figure is available in the online journal.)

PNe, being based on the independently determined distances to the Clouds, while in the Galactic case we use the statistical distance scale, which carries much larger, if reasonable, uncertainties. Nonetheless, the qualitative behavior or the CRD PNe in the two samples is similar in this plot, indicating a possible similarity of dust evolution in very different metallicity environments. By comparing the linear radii, we see that we are sampling comparable expansion phases (assuming homogeneous expansion velocities), with the notable difference of few Galactic PNe of very small radii; this is sensible if we recall that the Galactic PNe of the present sample were selected to be compact, unevolved ones. In spite of the uncertainties and the caveats associated with adopting a simple, blackbody temperature for the dust continuum, we note that the correlations for CRD PNe are very good if considered separately for each host galaxy, with the temperatures in the Magellanic Cloud sample being higher than in the Galactic sample at the same radii. The slope of the correlation is slightly higher in the Magellanic Cloud ($T_{dust} \propto R_{PN}^{-0.32}$) than in the Galactic ($T_{dust} \propto R_{PN}^{-0.25}$) case; in both cases, the correlation is tight, with a correlation coefficient of -0.99 and -0.75 for the Galactic disk and the Magellanic Cloud PNe, respectively. If we assume that the expansion rates are uniform in two samples, then we conclude that, at similar evolutionary stages, Magellanic PNe have higher dust temperatures than Galactic counterparts. If we assume that most CRD PNe have a similar progenitor mass and metallicity (in each of the two samples shown here), then we can conclude that the cooling of PN dust depends on the metallicity of the population. In particular, if the PN dust grains in the Magellanic Clouds are smaller than those in Galactic PNe due to metallicity, as seen in the ISM (e.g., Sandstrom et al. 2012), they are expected to retain higher dust temperatures (Li & Draine 2001), which is compatible with our analysis.

It is worth mentioning that the models of stellar evolution (Marigo et al. 1999; Karakas et al. 2003) predict that stars will experience the third dredge-up and the hot-bottom burning at lower masses for lower metallicities. There will therefore be a difference in the carbon-rich star progenitor masses for
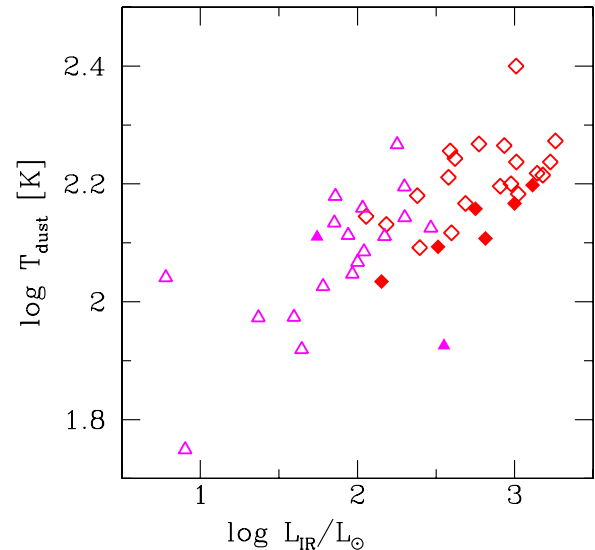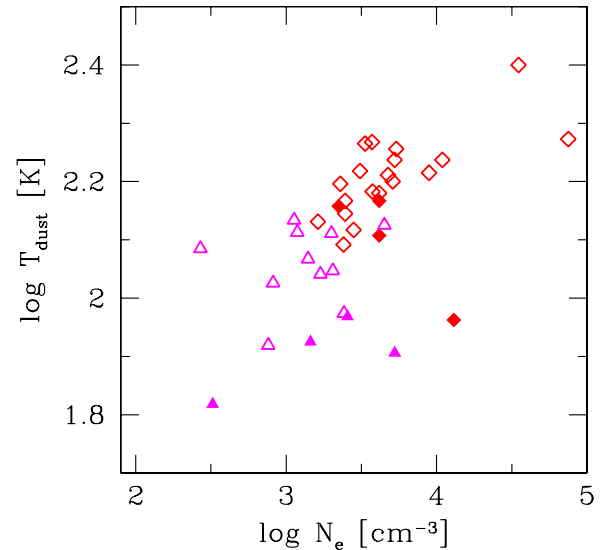
Galactic and Magellanic Cloud PNe. If the correlation between carbon abundances and carbon dust, demonstrated in Magellanic Cloud PNe by S07, will hold for the Galactic PNe as well, then the sequences of Galactic and Magellanic Cloud CRD PNe shown in Figure 14 could represent slightly different initial mass domains, which should then be taken into account in the comparison. To date, the sample of CRD Galactic PNe with a carbon abundance determination is way too small for such an analysis to be meaningful.

In Figure 15, we show the T_{dust} versus IR luminosity for the Galactic (filled symbols) and Magellanic Cloud (open symbols) PNe, and for the F and CRD PNe. Both Galactic and extragalactic CRD PNe seem to populate a sequence where high luminosity corresponds to high temperatures and vice versa. Galactic PNe have lower T_{dust} for similar luminosity, which we think is due to the metallicity effect on dust grain behavior, as illustrated above, implying the existence of smaller carbonaceous grains at low metallicity. Figure 16 shows the

relation of dust temperature with electron density, equally dense CRD PNe seem to have hotter dust in the Magellanic Cloud sample than the Galactic sample.

6. CONCLUSIONS

A large number of PNe with *Spitzer*/IRS spectra are presented in this paper. With the present sample, the early properties of ejected dust in Galactic PNe could be studied with sound statistical significance. The target sample includes all Galactic disk PNe with angular size smaller than ∼4 arcsec. A few targets turned out not to be bona fide PNe, leaving us with a pure sample of 150 Galactic PNe to study. All PN spectra show dust continua and nebular emission lines. Solid-state emission superimposed on the continuum displays a variety of characteristics. The dust classification, performed similarly to what we did for the Magellanic Cloud *Spitzer*/IRS spectra, consists of four major classes, determined by the type of dust that is prevalent in the spectra, including CRD, ORD, MCD, and featureless spectra PNe. Molecular/dust emission is much more apparent in this sample than in the Magellanic Cloud PNe, where featureless spectra with little or no continuum comprised a large fraction of the sample.

The most populated dust class in this Galactic sample is the ORD (or oxygen-rich dust) class, including PNe featuring crystalline and amorphous silicates, and a few which show both types of grains. The second most populated class is the mixed-chemistry PNe, where both carbon-rich and oxygen-rich dust features are evident above the dust continuum. In contrast, in the Magellanic Clouds the ORD PNe were a tiny minority, and MCD PNe were absent.

By separating the pure disk population and the possible bulge PNe within the present sample, we see that the bulge PNe are mostly of dual chemistry, as previously observed. Bulge, disk, and Magellanic Cloud PNe form a sequence where decreasing metallicity determines a decreasing fraction of ORD and MCD PNe, and an increasing fraction of CRD PNe.

Our analysis shows that CRD PNe define a rather narrow sequence when IR luminosity and physical radii are plotted against the dust temperature, which we interpret as an evolutionary sequence. The consequence of these findings is that CRD PNe must originate from progenitors with narrowly distributed mass, probably below ∼3 $M_\odot$, or, non-type I PNe (Peimbert 1978). ORD and MCD PNe might not display a similar sequence because oxygen-rich grains radiate more efficiently than their CRD counterparts and their dust temperatures are lower than those of CRD PNe.

When comparing the Galactic and Magellanic Cloud CRD PN, in particular their $T_{\rm dust}$ evolution and sequences, we find that dust temperatures are somewhat higher in the extragalactic than Galactic PNe for similar radii, which is in broad agreement with smaller carbonaceous dust grains observed at low metallicity in the ISM, and consequently possible smaller radiation efficiency in the Magellanic Cloud PNe than in their Galactic counterparts. Another likely explanation for the observed correlation is the effect of line blanketing at lower metallicity.

The data presented here have been already analyzed for the presence of some complex molecules, such as C_{60} (fullerene, García-Hernández et al. 2010). More molecular analysis is being performed at this time, as this represents the largest and most complete and homogeneous *Spitzer*/IRS Galactic PN data set available. We foresee that our group and others will take full advantage of the reduced data presented here for detailed future analysis of dust features.

REFERENCES

Acker, A., Marcout, J., Ochsenbein, F., et al. 1992, in The Strasbourg-ESO Catalogue of Galactic Planetary Nebulae, Parts I, II, ed. A. Acker, J. Marcout, F. Ochsenbein, B. Stenholm, R. Tylenda, & C. Schohn (Garching, Germany: European Southern Observatory), 1047
Bernard-Salas, J., Peeters, E., Sloan, G. C., et al. 2009, ApJ, 699, 1541
Cami, J., Bernard-Salas, J., Peeters, E., & Malek, S. E. 2010, Science, 329, 1180
Cioni, M.-R. L., Blommaert, J. A. D. L., Groenewegen, M. A. T., et al. 2003, A&A, 406, 51
Cioni, M.-R. L., & Habing, H. J. 2003, A&A, 402, 133
Cohen, M., & Barlow, M. J. 1974, ApJ, 193, 401
García-Hernández, D. A., García-Lario, P., Plez, B., et al. 2006, Science, 314, 1751
García-Hernández, D. A., García-Lario, P., Plez, B., et al. 2007a, A&A, 462, 711
García-Hernández, D. A., Iglesias-Groth, S., Acosta-Pulido, J. A., et al. 2011a, ApJ, 737, L30
García-Hernández, D. A., Manchado, A., García-Lario, P., et al. 2010, ApJ, 724, L39
García-Hernández, D. A., Manchado, A., Lambert, D. L., et al. 2009, ApJ, 705, L31
García-Hernández, D. A., Perea-Calderón, J. V., Bobrowsky, M., & García-Lario, P. 2007b, ApJ, 666, L33
García-Hernández, D. A., Rao, N. K., & Lambert, D. L. 2011b, ApJ, 729, 126
Grishko, V. I., Tereszchuk, K., Duley, W. W., & Bernath, P. 2001, ApJ, 558, L129
Groenewegen, M. A. T., Blommaert, J. A. D. L., Cioni, M.-R., et al. 2000, Mem. Soc. Astron. Ital., 71, 639
Gutenkunst, S., Bernard-Salas, J., Pottasch, S. R., Sloan, G. C., & Houck, J. R. 2008, ApJ, 680, 1206
Herwig, F. 2005, ARA&A, 43, 435
Higdon, S. J. U., Devost, D., Higdon, J. L., et al. 2004, PASP, 116, 975
Höfner, S. 2011, in ASP Conf. Ser. 445, Why Galaxies Care about AGB Stars II: Shining Examples and Common Inhabitants, ed. F. Kerschbaum, T. Lebzelter, & R. F. Wing (San Francisco, CA: ASP), 193
Hony, S., Waters, L. B. F. M., & Tielens, A. G. G. M. 2002, A&A, 390, 533
Karakas, A. I., Lattanzio, J. C., & Pols, O. R. 2003, in IAU Symp. 209, Planetary Nebulae: Their Evolution and Role in the Universe, ed. S. Kwok, M. Dopita, & R. Sutherland (San Francisco, CA: ASP), 82
Kerber, F., Mignani, R. P., Guglielmetti, F., & Wicenec, A. 2003, A&A, 408, 1029
Kwok, S., & Zhang, Y. 2011, Nature, 479, 80
Leger, A., & Puget, J. L. 1984, A&A, 137, L5
Lenzuni, P., Natta, A., & Panagia, N. 1989, ApJ, 345, 306
Li, A., & Draine, B. T. 2001, ApJ, 554, 778
Morgan, D. H. 1984, MNRAS, 208, 633
Marigo, P., Girardi, L., & Bressan, A. 1999, A&A, 344, 123
Parker, Q. A., Acker, A., Frew, D. J., et al. 2006, MNRAS, 373, 79
Peimbert, M. 1978, Planetary Nebulae, Vol. 76 (Dordrecht: Reidel), 215
Perea-Calderón, J. V., García-Hernández, D. A., García-Lario, P., Szczerba, R., & Bobrowsky, M. 2009, A&A, 495, L5
Pottasch, S. R. 1984, Planetary Nebulae - A Study of Late Stages of Stellar Evolution (Astrophysics and Space Science Library, Vol. 107; Dordrecht: Reidel)
Sandstrom, K. M., Bolatto, A. D., Bot, C., et al. 2012, ApJ, 744, 20
Schultheis, M., Glass, I. S., & Cioni, M.-R. 2004, A&A, 427, 945
Scott, A., & Duley, W. W. 1996, ApJ, 472, L123
Scott, A., Duley, W. W., & Pinho, G. P. 1997, ApJ, 489, L193
Shaw, R. A., & Dufour, R. J. 1995, PASP, 107, 896
Sloan, G. C., Kraemer, K. E., Wood, P. R., et al. 2008, ApJ, 686, 1056

Speck, A. K., Corman, A. B., Wakeman, K., Wheeler, C. B., & Thompson, G. 2009, ApJ, 691, 1202

Stanghellini, L., García-Lario, P., García-Hernández, D. A., et al. 2007, ApJ, 671, 1669 (S07)

Stanghellini, L., & Haywood, M. 2010, ApJ, 714, 1096

Stanghellini, L., & Renzini, A. 2000, ApJ, 542, 308

Stanghellini, L., Shaw, R. A., & Villaver, E. 2008, ApJ, 689, 194

Stanghellini, L., Villaver, E., Manchado, A., & Guerrero, M. A. 2002, ApJ, 576, 285

Trams, N. R., van Loon, J. Th., Waters, L. B. F. M., et al. 1999, A&A, 346, 843

Villaver, E., García-Segura, G., & Manchado, A. 2002a, ApJ, 571, 880

Villaver, E., Manchado, A., & García-Segura, G. 2002b, ApJ, 581, 1204

Waters, L. B. F. M., Beintema, D. A., Zijlstra, A. A., et al. 1998, A&A, 331, L61

Weidmann, W. A., & Gamen, R. 2011, A&A, 526, A6

Yamamura, I., Makiuti, S., Ikeda, N., et al. 2010, AKARI-FIS Bright Source Catalogue Release Note, Version 1.0

Zhang, C. Y., & Kwok, S. 1991, A&A, 250, 179

Zhang, K., Jiang, B. W., & Li, A. 2009, ApJ, 702, 680

Zoccali, M., Lecureur, A., Barbuy, B., et al. 2006, A&A, 457, L1